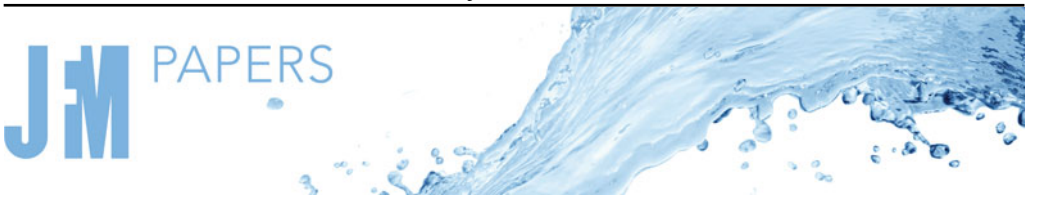
J. Fluid Mech. (2025), *vol.* 1024, A59, doi:10.1017/jfm.2025.10930



Mean flow generation via non-resonant interactions in two-dimensional forced stratified turbulence

Antonin Zoppi[1], **Paul Billant**[1] **and Leo Demaine**[1]

[1]LadHyX, CNRS, Ecole Polytechnique, Institut Polytechnique de Paris, 91120 Palaiseau, France

Corresponding author: Paul Billant, paul.billant@ladhyx.polytechnique.fr

(Received 16 January 2025; revised 27 July 2025; accepted 30 October 2025)

We perform numerical simulations of two-dimensional strongly stratified flows in a square periodic domain (y, z) forced by a steady mode with vorticity of the form $\sin(k_{yf}y)\sin(k_{zf}z)$, where (k_{yf}, k_{zf}) are fixed wavenumbers. It is shown that such deterministic forcing can lead to a transition to turbulence and the emergence of horizontal layers (so-called vertically sheared horizontal flows, VSHFs) similarly as for random stochastic forcing. The flow characteristics are studied depending on the Froude and Reynolds numbers. Furthermore, the mechanisms of layers formation are disentangled. Triadic instabilities first lead to the growth of pairs of wavevectors that resonate with each of the four forced wavevectors. Quadratic interactions between these resonant modes and the forcing also drive the growth of several non-resonant modes at the same growth rate. Since the forcing comprises the wavevectors $\pm(k_{yf}, k_{zf})$ and their mirror symmetric with respect to the horizontal $\pm(k_{yf}, -k_{zf})$, there exist enslaved/bound modes with the same horizontal wavenumber and different vertical wavenumbers. Hence, the quadratic interactions between the latter modes force a second generation of modes among which some are VSHFs. Their growth rate is twice the growth rate of the primary resonant modes. Such a mechanism is similar to resonant quartets (Newell, *J. Fluid Mech.*, 1969, vol. 35, no 2, pp. 255–271; Smith & Waleffe, *Phys. Fluids*, 1999, vol. 11, no 6, pp. 1608–1622). When the forcing is restricted to only the two wavevectors $\pm(k_{yf}, k_{zf})$, the second generation of enslaved/bound modes all have a non-zero horizontal wavenumber. However, further quadratic interactions can force VSHF. Thus, horizontal layers also emerge, but with a growth rate equal to the number of quadratic interactions times the growth rate of the primary instability.

Key words: stratified flows, stratified turbulence, transition to turbulence

© The Author(s), 2025. Published by Cambridge University Press.

https://doi.org/10.1017/jfm.2025.10930 Published online by Cambridge University Press

1. Introduction

Quasi-horizontal layers are ubiquitous in stably stratified flows (Riley & Lelong 2000; Caulfield 2021). In the case of numerical simulations of forced stratified turbulence in periodic domains, the layers take the form of the so-called 'shear modes' or 'vertically sheared horizontal flows' (VSHFs), i.e. horizontal flows purely uniform along the horizontal and varying only along the vertical (Smith 2001; Smith & Waleffe 2002). These shear modes usually grow slowly over a long time scale when using periodic boundary conditions both in three-dimensional (Herring & Métais 1989; Laval, McWilliams & Dubrulle 2003; Waite & Bartello 2004; Lindborg 2006; Brethouwer *et al.* 2007; Augier, Billant & Chomaz 2015; Herbert *et al.* 2016; Maffioli, Brethouwer & Lindborg 2016) and two-dimensional numerical simulations of stratified turbulence (Smith 2001; Remmel, Sukhatme & Smith 2014; Kumar, Verma & Sukhatme 2017; Fitzgerald & Farrell 2018*a*, 2018*b*; Linares 2020). Numerical simulations are often interrupted before shear modes become too dominant or, in some cases, they are even artificially suppressed. Several mechanisms have been proposed to explain their origin such as waves interactions (Smith 2001; Smith & Waleffe 2002; Remmel *et al.* 2014), viscous effects (Lindborg 2006) or statistical instability of homogeneous stratified turbulence (Fitzgerald & Farrell 2018*a*, 2018*b*).

Similar mean flows varying in only one or two directions are observed in a variety of other contexts such as rotating turbulence (Smith & Waleffe 1999), stratified-rotating turbulence (Smith & Waleffe 2002) and turbulence on the β-plane (Rhines 1975; Smith & Waleffe 1999; Galperin & Read 2019; Lemasquerier, Favier & Le Bars 2021). All these fluids can sustain plane waves in an infinite medium and the mean flow corresponds to a zero frequency wave or mode. However, it is well known that such a slow wave or mode cannot be directly generated by resonant triad interactions involving two other waves since the coefficient of interaction vanishes for zero frequency (see Phillips (1968), McEwan, Mander & Smith (1972) and Lelong & Riley (1991) for the case of stratified fluids). Other plausible mechanisms, such as near-resonant triads and resonant quartets of waves, have been therefore invoked to explain a transfer into a zero frequency wave (Newell 1969; Smith & Waleffe 1999). In particular, it has been shown that a geostrophic flow in rotating flows can be generated by a near-resonant instability of a single inertial wave (Le Reun *et al.* 2020) or by a secondary quartetic instability of the triadic instability in turbulence driven by a wave forcing (Brunet, Gallet & Cortet 2020). Alternatively, the emergence of a mean flow in geostrophic turbulence or two-dimensional stratified turbulence has been explained in terms of a zonostrophic instability that breaks the statistical homogeneity of turbulence (Srinivasan & Young 2012; Fitzgerald & Farrell 2018*a*, 2018*b*; Farrell & Ioannou 2019). This framework shows indeed that, statistically, there is a positive feedback between the fluctuating turbulent Reynolds stresses and the mean flow.

In contrast to the latter statistical approach, which relies on a stochastic forcing of the turbulence, Lemasquerier *et al.* (2021) have studied experimentally and numerically β-plane flows generated by a steady forcing. Interestingly, they have shown that the resulting flows are also turbulent and exhibit a zonal mean flow. This suggests that the mechanisms responsible for the emergence of a mean flow could be understood in the simple case of a deterministic forcing. With this in mind, we study herein two-dimensional stratified flows generated by a steady forcing with a single wavenumber in each direction. This differs from previous studies of two-dimensional stratified turbulence that was randomly forced within a given range of small or large wavenumbers (Smith 2001; Kumar *et al.* 2017; Fitzgerald & Farrell 2018*a*; Linares 2020). Despite this difference, we will see that the present steady forcing also leads to a transition to a turbulent flow that

https://doi.org/10.1017/jfm.2025.10930 Published online by Cambridge University Press

exhibits a power-law spectrum and shear modes. The advantage of a deterministic forcing compared with a random forcing is that it will enable us to disentangle the chronology of events leading to the transition to turbulence and the emergence of shear modes.

Such evolution towards turbulence is not unexpected since it has been shown that the breaking of a single two-dimensional internal wave can lead to stratified turbulence (Bouruet-Aubertot *et al.* 1995, 1996; Benielli & Sommeria 1998; Staquet & Sommeria 2002; Koudella & Staquet 2006; Dauxois *et al.* 2018). Furthermore, while a single monochromatic internal plane progressive wave cannot induce a mean flow, an inhomogeneous internal wave or the interaction between several monochromatic waves may generate a mean flow (Galmiche, Thual & Bonneton 2000; Sutherland 2010; Semin *et al.* 2016; Dauxois *et al.* 2018). The quasi-biennial oscillation of the wind in the stratosphere is one of the most famous examples of mean flow induced by waves (Plumb & McEwan 1978; Wedi & Smolarkiewicz 2006; Semin *et al.* 2018). In the present configuration, we will see that the mean flow is induced by non-resonant interactions between different modes similarly as observed by Galmiche *et al.* (2000).

The paper is organised as follows. Section 2 presents the governing equations, the forcing with two pairs of wavevectors $\pm(k_{yf}, \pm k_{zf})$ and the numerical methods. A typical numerical simulation is first described in § 3. The main effects of the control parameters (forcing amplitude, buoyancy frequency and viscosity) are then investigated in § 4. In § 5, we unravel the mechanisms responsible for the transition to turbulence and the generation of an horizontal mean flow. Numerical simulations for various wavenumbers of the forcing are presented and analysed in § 6. Finally, § 7 describes a simulation in which the forcing has been truncated to a single pair of wavevectors $\pm(k_{yf}, k_{zf})$. Turbulence and shear modes also arise, but through a mechanism slightly different from the one evidenced in § 5. The conclusions are drawn in § 8.

2. Problem formulation and numerical methods

We use the two-dimensional incompressible Navier–Stokes equations under the Boussinesq approximation:

$$\frac{\partial \boldsymbol{u}}{\partial t} + (\boldsymbol{u}\cdot\boldsymbol{\nabla})\boldsymbol{u} = -\boldsymbol{\nabla}\left(\frac{p}{\rho_0}\right) + b\boldsymbol{e_z} + \nu\Delta\boldsymbol{u} + \boldsymbol{F}, \tag{2.1a}$$

$$\frac{\partial b}{\partial t} + \boldsymbol{u}\cdot\boldsymbol{\nabla} b = -N^2 w + \kappa\Delta b, \tag{2.1b}$$

$$\boldsymbol{\nabla}\cdot\boldsymbol{u} = 0, \tag{2.1c}$$

where $\boldsymbol{u} = (v, w)$ is the velocity field in Cartesian coordinates $\boldsymbol{x} = (y, z)$, p the pressure, $b = -g\rho'/\rho_0$ the buoyancy with g the gravity, ρ' the density perturbation and ρ_0 the reference density. Here, $\boldsymbol{e_z}$ is the vertical unit vector pointing upward, $\boldsymbol{F}$ the forcing, $N = \sqrt{-(g/\rho_0)\partial\bar{\rho}/\partial z}$ the Brunt–Väisälä frequency with $\bar{\rho}(z)$ the mean density profile. Additionally, ν is the viscosity and κ the diffusivity of the stratifying agent. The Schmidt number $S_c = \nu/\kappa$ will always be set to unity in the following.

The forcing is solenoidal with an horizontal vorticity $q = (\boldsymbol{\nabla}\times\boldsymbol{F}).\boldsymbol{e_x}$ taken as a steady mode with a single wavenumber in each direction:

$$q(y, z) = q_0 \sin(k_{yf}y)\sin(k_{zf}z), \tag{2.2}$$

where q_0 is the amplitude and (k_{yf}, k_{zf}) the wavenumbers of the forcing, which will be assumed positive without loss of generality. Alternatively, (2.2) can be written

https://doi.org/10.1017/jfm.2025.10930 Published online by Cambridge University Press

as the superposition of four wavevectors: $q = (q_0/4)(\exp(\mathrm{i}\boldsymbol{k}_{f-}\cdot\boldsymbol{x}) + \exp(-\mathrm{i}\boldsymbol{k}_{f-}\cdot\boldsymbol{x}) - \exp(\mathrm{i}\boldsymbol{k}_{f+}\cdot\boldsymbol{x}) - \exp(-\mathrm{i}\boldsymbol{k}_{f+}\cdot\boldsymbol{x}))$, where

$$\boldsymbol{k}_{f+} = (k_{yf}, k_{zf}), \quad \boldsymbol{k}_{f-} = (k_{yf}, -k_{zf}). \tag{2.3}$$

The subscripts $+$ and $-$ will be convenient in the following to distinguish the different forced wavevectors.

If the velocity $\boldsymbol{u}$ and buoyancy b are initially null, the response to (2.2) can be determined asymptotically for small amplitude q_0 as is done by Thorpe (1968) and Bouruet-Aubertot, Sommeria & Staquet (1995) for a standing wave. At leading order, this yields:

$$b = q_0\left[\beta + e^{-ct}\left(a\sin\Omega t - \beta\cos\Omega t\right)\right]\cos(k_{yf}y)\sin(k_{zf}z) + O(q_0^2), \tag{2.4a}$$

$$\psi = q_0\left[\gamma + e^{-ct}\left(\mu\sin\Omega t - \gamma\cos\Omega t\right)\right]\sin(k_{yf}y)\sin(k_{zf}z) + O(q_0^3), \tag{2.4b}$$

where ψ is a streamfunction such that $v = -\partial\psi/\partial z$, $w = \partial\psi/\partial y$ and

$$\begin{gathered}
\Omega = \sqrt{\frac{N^2k_{yf}^2}{k_f^2} - \frac{1}{4}\left(1 - \frac{1}{S_c}\right)^2\nu^2k_f^4}, \quad c = \frac{1}{2}\left(1 + \frac{1}{S_c}\right)\nu k_f^2, \\
\beta = \left[k_{yf}\left(1 + \frac{\nu^2}{N^2S_c}\frac{k_f^6}{k_{yf}^2}\right)\right]^{-1}, \qquad \gamma = -\frac{\nu k_f^2\beta}{N^2S_ck_{yf}}, \\
a = -\frac{\beta c}{\Omega}, \qquad \mu = -\frac{\beta k_{yf}}{\Omega k_f^2}\left[1 - \frac{\nu^2k_f^4}{N^2k_{yf}^2S_c}\left(1 - \frac{1}{S_c}\right)\right],
\end{gathered} \tag{2.5}$$

where $k_f^2 = k_{yf}^2 + k_{zf}^2$. The parameters Ω and c correspond to the real and imaginary parts of the frequency of internal waves in the presence of dissipative effects. Since $S_c = 1$, Ω recovers the dispersion relation in the inviscid limit. At the next order, the buoyancy is of the form $q_0^2 f(t)\sin 2k_{zf}z$, whereas ψ is of the form $q_0^3\sin(k_{yf}y)[g(t)\sin(3k_{zf}z) + h(t)\sin(k_{zf}z)]$, where f, g and h are functions of time (not given here). Hence, the horizontally averaged buoyancy is non-zero at order q_0^2 with a vertical wavenumber $2k_{zf}$. This comes from the advection of buoyancy in (2.1*b*). A similar feature occurs for a standing internal wave (Thorpe 1968; Bouruet-Aubertot *et al.* 1995). However, by noticing that (2.1) is invariant under the change $y \to -y$, $b \to b$, $\psi \to -\psi$, it can be deduced that the streamfunction should be an odd function of y implying that the horizontally averaged streamfunction is zero at any order in q_0. In other words, there is no mean horizontal flow directly forced by (2.2).

The solution (2.4) shows that b and ψ oscillate at the frequency Ω, but become steady as $t \to \infty$ since the time-dependent terms decay due to dissipation. The streamfunction is then proportional to $q_0\gamma \propto q_0\nu/N^2$, whereas the buoyancy scales as q_0. An example of the evolution of b and ψ will be presented at the end of this section. In any case, in the following numerical simulations, we will see that the flow will depart from (2.4) because the initial velocity field will not be strictly null, but will consist of a divergence-free random noise of amplitude 0.01.

The Froude number F_h and Reynolds number Re are defined thanks to the characteristics of the forcing as follows:

$$F_h = \frac{\sqrt{q_0}}{N}, \qquad Re = \frac{\sqrt{q_0}l_0^2}{\nu}, \tag{2.6}$$

with $l_0 = 2\pi/k_{yf}$ the horizontal wavelength of the forcing.

https://doi.org/10.1017/jfm.2025.10930 Published online by Cambridge University Press

Re	F_h	ν	N	q_0	(k_{yf}, k_{zf})	T_f	$k_{max}\eta$	F_{ht}	Re_t	Re_b
3590	0.16	0.008	1.75	0.083	$(4k_0, 4k_0)$	5.08	5.2	0.015	331	0.08
7180	0.33	0.008	1.75	0.33	$(4k_0, 4k_0)$	5.08	2.3	0.044	965	1.88
8840	0.40	0.008	1.75	0.50	$(4k_0, 4k_0)$	5.08	1.8	0.060	1308	4.68
9520	0.43	0.008	1.75	0.58	$(4k_0, 4k_0)$	5.08	1.7	0.068	1480	6.78
11 920	0.54	0.008	1.75	0.91	$(4k_0, 4k_0)$	5.08	1.5	0.076	1680	9.87
11 790	0.40	0.006	1.75	0.50	$(4k_0, 4k_0)$	5.08	1.5	0.058	1680	5.58
7070	0.40	0.01	1.75	0.50	$(4k_0, 4k_0)$	5.08	2.1	0.061	1070	4.02
8840	0.47	0.008	1.5	0.50	$(4k_0, 4k_0)$	5.92	1.9	0.066	1240	5.36
8840	0.35	0.008	2	0.50	$(4k_0, 4k_0)$	4.44	2.0	0.046	1140	2.39
8840	0.31	0.008	2.25	0.50	$(4k_0, 4k_0)$	3.95	1.9	0.043	1220	2.32
8840	0.28	0.008	2.5	0.50	$(4k_0, 4k_0)$	3.55	2.5	0.028	880	0.70
15 710	0.40	0.008	1.75	0.50	$(3k_0, 3k_0)$	5.08	1.8	0.050	2000	4.96
8840	0.40	0.008	1.75	0.50	$(4k_0, 3k_0)$	4.49	—	—	—	—
8840	0.40	0.008	1.75	0.50	$(4k_0, 5k_0)$	5.75	2.2	0.048	1050	2.41
5660	0.40	0.008	1.75	0.50	$(5k_0, 4k_0)$	4.60	3.9	0.025	353	0.22

Table 1. Summary of the parameters of the main simulations. Re and F_h are the Reynolds and Froude numbers, respectively, as defined in (2.6). ν is the viscosity, N the Brunt–Väisälä frequency, q_0 the amplitude of the forcing, (k_{yf}, k_{zf}) the wavenumbers of the forcing and $T_f = 2\pi/\Omega$. k_{max} is the maximum wavenumber and η is the Kolmogorov length scale. F_{ht}, Re_t and Re_b are respectively the turbulent Froude number, Reynolds number and buoyancy Reynolds number defined in (2.7).

Equations (2.1*a*)–(2.1*c*) are solved by means of a pseudo-spectral method with periodic boundary conditions (Deloncle 2007; Deloncle, Billant & Chomaz 2008). Time stepping is performed by a fourth-order Runge–Kutta scheme. Aliasing is removed by using a truncation radius of 2/3.

The numerical domain has been taken as a square with size $L_y = L_z = 40$ and with a resolution $N_y = N_z = 512$. In most of the simulations, the wavenumbers of the forcing have been set to $k_{yf} = k_{zf} = 4k_0$, where $k_0 = 2\pi/L_y$ is the lowest non-zero wavenumber. In other words, the forcing has four wavelengths in each direction. However, different forcing wavenumbers will be investigated in § 6.

The Brunt–Väisälä frequency, the viscosity and the amplitude of the forcing have been varied in the ranges: $1.5 \leqslant N \leqslant 2.5$, $0.006 \leqslant \nu \leqslant 0.01$ and $0.083 \leqslant q_0 \leqslant 0.91$ (table 1). The corresponding Froude and Reynolds numbers are respectively small and large, in the ranges: $0.16 < F_h < 0.54$, $3580 < Re < 15\,710$.

For comparison purpose, table 1 also indicates the turbulent Froude, Reynolds and buoyancy Reynolds numbers defined as follows:

$$F_{ht} = \frac{\epsilon_m^{1/3}}{N l_0^{2/3}}, \qquad Re_t = \frac{\epsilon_m^{1/3} l_0^{4/3}}{\nu}, \qquad Re_b = \frac{\epsilon_m}{\nu N^2}, \tag{2.7}$$

where $\epsilon_m = \max(\epsilon)$ with ϵ the dissipation rate of kinetic energy averaged over the domain. These definitions are equivalent to those of Brethouwer *et al.* (2007) and Maffioli (2019) based on the root mean square of the horizontal velocity fluctuations U instead of l_0 if the Taylor's relation $\epsilon_m \sim U^3/l_0$ holds (Lindborg 2006). As seen in table 1, all the simulations have a Froude number $F_{ht} = O(10^{-2})$ and most of them have a buoyancy Reynolds number larger than unity indicating that they correspond to the strongly stratified turbulent regime: $F_{ht} \ll 1$, $Re_b > 1$ (Brethouwer *et al.* 2007).

The numerical parameters always satisfy the criterion $k_{max}\eta > 1$ (table 1) required for direct numerical simulations, where $k_{max} = N_y k_0/2$ is the maximum wavenumber and

https://doi.org/10.1017/jfm.2025.10930 Published online by Cambridge University Press

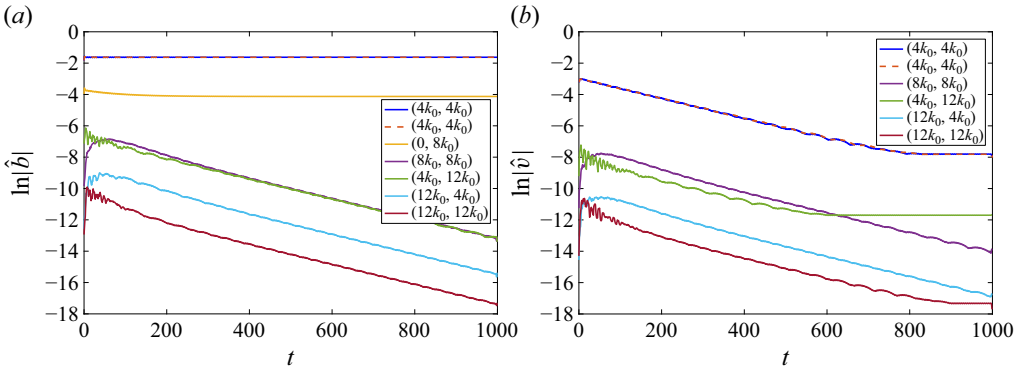


Figure 1. Evolution of the amplitudes of the modes in the wavenumber ranges $0 \leqslant k_y \leqslant 12k_0$, $0 \leqslant k_z \leqslant 12k_0$ of the (a) buoyancy b and (b) horizontal velocity v in a simulation without random noise at $t = 0$ for $F_h = 0.4$, $Re = 8840$ and $k_{yf} = k_{zf} = 4k_0$ (solid lines). The dashed lines represent the asymptotic solution (2.4). The y-axis corresponds to natural logarithm. A moving average over a time interval $\Delta t = 5$ has been applied to filter the oscillations at frequency Ω.

$\eta = \nu^{3/4}/\epsilon_m^{1/4}$ the Kolmogorov scale (de Bruyn Kops & Riley 1998). The time step Δt has been set to 10^{-3} to guarantee the Courant–Friedrichs–Lewy condition. The convergence of the simulations has been tested by running a simulation with the resolution $N_y = N_z = 1024$ for one set of parameters and by checking that it gives similar results as with $N_y = N_z = 512$.

To check and illustrate the asymptotic solution (2.4), a control simulation has been first performed with a zero initial velocity and buoyancy fields for $F_h = 0.4$, $Re = 8840$ and $k_{yf} = k_{zf} = 4k_0$. Figure 1 shows the evolution of the amplitudes $\hat{b}$ and $\hat{v}$ (solid lines) of the Fourier modes of the buoyancy and the horizontal velocity component, i.e.

$$b = \sum_{\boldsymbol{k}} \hat{b}(t, \boldsymbol{k}) e^{\mathrm{i}k_y y + \mathrm{i}k_z z}, \qquad v = \sum_{\boldsymbol{k}} \hat{v}(t, \boldsymbol{k}) e^{\mathrm{i}k_y y + \mathrm{i}k_z z}, \tag{2.8}$$

which are non-zero in the wavenumber bands: $0 \leqslant k_y \leqslant 12k_0$, $0 \leqslant k_z \leqslant 12k_0$. For clarity, a moving average over a time interval $\Delta t = 5$ has been applied to smooth oscillations with period $T_f = 2\pi/\Omega = 5.08$. Note that the curves do not vanish at $t = 0$ because of this moving average. The amplitude of the Fourier mode $(k_y, k_z) = (4k_0, 4k_0)$ of the leading order asymptotic solution (2.4) is also represented by orange dashed lines and is in excellent agreement with the corresponding Fourier mode in the simulation (blue solid lines). As can be seen in figure 1(a), the dominant Fourier mode of b converges quickly to the steady value $q_0\beta/4$ (see (2.4a)). In contrast, according to (2.4b), the dominant mode of v (figure 1b) decreases slowly by dissipation from the initial value $q_0\mu k_{zf}/4$, which is of order unity, towards the steady amplitude $q_0\gamma k_{zf}/4$. The latter value is small since it is proportional to the viscosity ν and is reached only after $t = 800$. The slow modulations visible on this curve and other ones are due to the combined effect of the moving average and the fact that the fields are saved with the sampling period $\Delta t_s = 1$. The other Fourier modes that are generated at the next orders in the expansion with q_0 are all much smaller except the mode $(0, 8k_0)$ for b (red line in figure 1a), which corresponds to the second-order term in (2.4a) ($q_0^2 f(t) \sin(2k_{zf}z)$). Figure 1($b$) confirms that the forcing does not generate any mode for v with zero horizontal wavenumber and non-zero vertical wavenumber, i.e. VSHF.

https://doi.org/10.1017/jfm.2025.10930 Published online by Cambridge University Press

3. Description of a typical simulation

3.1. *Global evolution*

We first describe the main features of the simulation for $F_h = 0.4$, $Re = 8840$ and $k_{yf} = k_{zf} = 4k_0$, corresponding to the dimensional parameters $q_0 = 0.5$, $\nu = 0.008$, $N = 1.75$ (table 1). We recall that the velocity field is now initialised by a small random noise. Figure 2 displays the horizontal velocity component v at different times. At early stages (figure 2*a*), the flow has exactly the same shape as the forced flow (2.4). At $t = 410$, this regular structure becomes modulated and exhibits inclined bands (figure 2*b*) indicating the emergence of modes different from the forced ones. Later on, at $t = 560$ (figure 2*c*), the velocity field becomes irregular at small scales although some periodicities are still present at large scales. A series of eight horizontal layers with alternate sign then arise (figure 2*d* at $t = 1100$). The vertical wavelength of this layered pattern is the same as that of the forcing. However, by $t = 2100$ (figure 2*e*) and $t = 4630$ (figure 2*f*), some layers have disappeared, while others have intensified and thickened so that they are no longer regularly alternated.

Such flow structure and evolution strongly resemble two-dimensional stratified turbulence generated by random forcing (Smith 2001; Kumar *et al.* 2017; Fitzgerald & Farrell 2018*a*; Linares 2020). The turbulent character of the flow is further evidenced in figure 3, which displays one-dimensional horizontal and vertical spectra of kinetic and potential energies around $t = 2100$. As observed in the aforementioned studies of two-dimensional stratified turbulence, the spectra exhibit power-law behaviours with a slope closer to -3 (purple line) than $-5/3$ (green line). We can notice that the vertical kinetic energy spectrum around the forced wavenumber is larger than the horizontal kinetic energy spectrum reflecting the presence of the horizontal layers. At high wavenumbers, the vertical and horizontal spectra are closer indicating that velocity fluctuations at small scales are more isotropic.

To analyse the emergence and global evolution of the mean flow, the velocity component v has been decomposed into its mean part $\langle v \rangle_y$ (corresponding to shear modes $\hat{v}(t, k_y = 0, k_z)$ in Fourier space) and its fluctuations v':

$$v = \langle v \rangle_y + v', \tag{3.1}$$

where $\langle \cdot \rangle_a$ denotes the average along the direction a. Figure 4 first displays a space–time diagram of $\langle v \rangle_y(z, t)$. The layers become clearly visible around $t \approx 600$ and start to be strongly irregular after $t \approx 2000$. Figure 5 shows the root mean square (r.m.s.) of each of the three quantities v, $\langle v \rangle_y$, v', where the r.m.s. of a quantity X is defined as $X_{rms} = \sqrt{\langle X^2 \rangle_{y,z}}$. The r.m.s. of the vertical velocity w and of the scaled buoyancy b/N are also plotted with purple and orange lines, respectively. Until $t \approx 400$, v_{rms} is small and follows the solution (2.4). However, an exponential increase of v_{rms} occurs subsequently. During this exponential phase, v_{rms} consists initially only in fluctuations, i.e. the mean flow $\langle v \rangle_{y-rms}$ is zero. Somewhat later, around $t \approx 500$, it also starts to grow exponentially. However, the inset in figure 5 shows that the growth rate of $\langle v \rangle_{y-rms}$ is twice that of v'_{rms}, which has been estimated as follows:

$$\sigma = \frac{1}{t_2 - t_1} \ln \left(\frac{v'_{rms}(t_2)}{v'_{rms}(t_1)} \right), \tag{3.2}$$

where t_2 and t_1 are two sufficiently distinct times chosen during the regime of pure exponential growth. After $t \gtrsim 800$, $\langle v \rangle_{y-rms}$ becomes larger than the fluctuating part v'_{rms}. The latter saturates after $t \approx 700$, whereas the r.m.s. of the mean flow saturates only later, for $t \gtrsim 1200$. The r.m.s. of the vertical velocity w_{rms} is of the same order as v'_{rms}.

https://doi.org/10.1017/jfm.2025.10930 Published online by Cambridge University Press

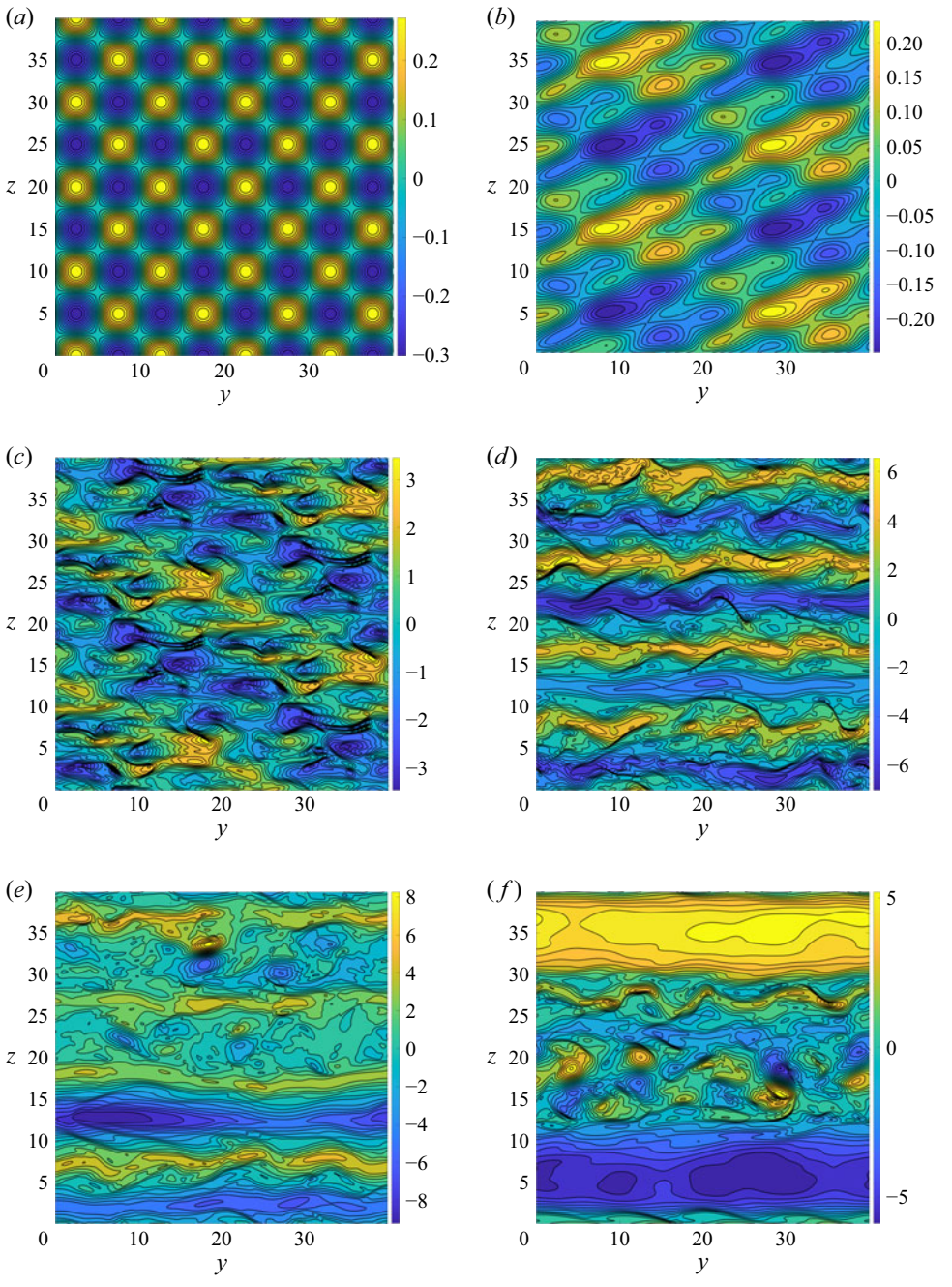


Figure 2. Horizontal velocity field v for $Re = 8840$, $F_h = 0.4$ and $k_{yf} = k_{zf} = 4k_0$ at different times: (*a*) $t = 1$; (*b*) $t = 410$; (*c*) $t = 560$; (*d*) $t = 1100$; (*e*) $t = 2100$; (*f*) $t = 4630$.

Hence, the fluctuating turbulent motions seem isotropic despite of the stable stratification. This is probably due to the fact that the forcing is isotropic and is present both in the horizontal and vertical momentum (2.1*a*).

In contrast, the r.m.s. of the scaled buoyancy b_{rms}/N (orange line) exhibits large amplitude oscillations over a very long period around 2000−3000 time units. A first cycle

https://doi.org/10.1017/jfm.2025.10930 Published online by Cambridge University Press

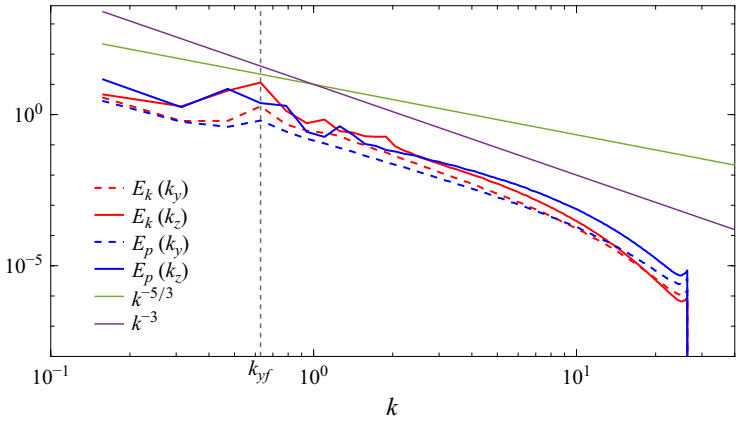


Figure 3. One-dimensional spectra of kinetic energy E_k (red lines) and potential energy E_p (blue lines) for $Re = 8840$, $F_h = 0.4$ and $k_{yf} = k_{zf} = 4k_0$ averaged over the time interval $2100 \leqslant t \leqslant 2200$. The solid and dashed lines show the horizontal and vertical spectra, respectively. The purple and green lines represent the k^{-3} and $k^{-5/3}$ slopes, respectively. The vertical dashed line indicates the forced wavenumber $k_{yf} = k_{zf}$.

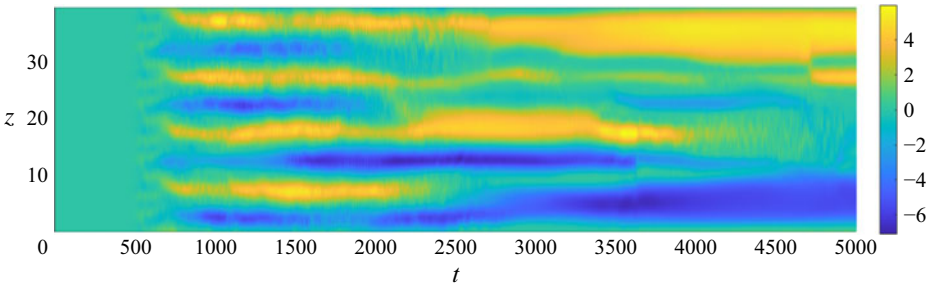


Figure 4. Space–time diagram of the horizontal mean flow $\langle v \rangle_y(z, t)$ for $Re = 8840$, $F_h = 0.4$ and $k_{yf} = k_{zf} = 4k_0$.

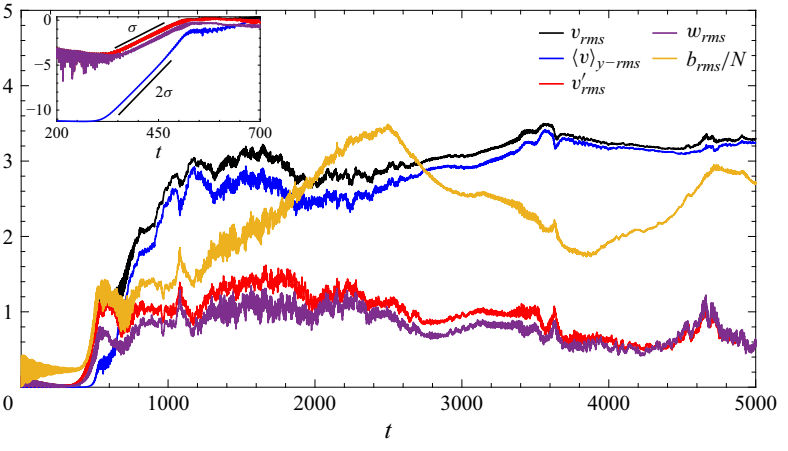


Figure 5. Temporal evolution of the root mean square of the total horizontal velocity v, the mean $\langle v \rangle_y$, the fluctuations v', the vertical velocity w and the scaled buoyancy b/N for $F_h = 0.4$, $Re = 8840$ and $k_{yf} = k_{zf} = 4k_0$. The inset shows a close-up view of the curves of $\langle v \rangle_{y-rms}$, v'_{rms} and w_{rms} plotted in natural logarithm coordinate in the range $200 \leqslant t \leqslant 700$. The black straight lines represent the slopes of pure exponential growth at rates σ and 2σ.

https://doi.org/10.1017/jfm.2025.10930 Published online by Cambridge University Press

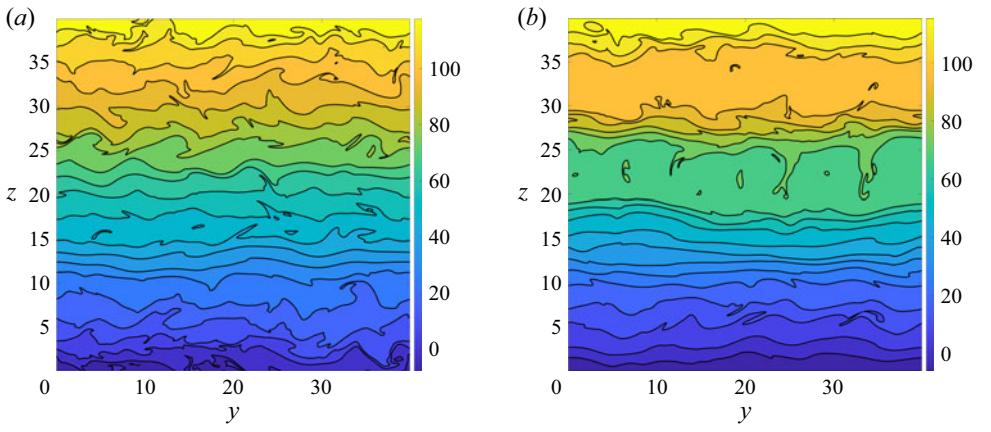


Figure 6. Total buoyancy field $b_t = N^2 z + b$ for $Re = 8840$, $F_h = 0.4$ and $k_{yf} = k_{zf} = 4k_0$ at different times: (*a*) $t = 1100$; (*b*) $t = 2100$.

of oscillation occurs between $t \approx 1000$ and $t \approx 3800$, while we can see half of the second cycle between $t \approx 3800$ and $t \approx 4700$. Such behaviour can be understood by examining the total buoyancy field $b_t = N^2 z + b$ around a minimum and a maximum of b_{rms}/N: $t = 1100$ (figure 6*a*) and $t = 2100$ (figure 6*b*). The corresponding horizontal velocity field at these two instants were displayed in figure 2(*d–e*).

Near a minimum of b_{rms}/N, the iso-buoyancy lines are approximately equi-spaced along the vertical (figure 6*a*), i.e. there are no large buoyancy fluctuations b. In contrast, around a maximum of b_{rms}/N, the mean vertical gradient of b_t is irregular: two regions of low gradient can be seen in the upper part of the domain (figure 6*b*). Then, b_{rms}/N is high since the buoyancy b exhibits fluctuations as large as the base buoyancy field $N^2 z$. This corresponds to the regions where vortices (looking like a dipole pattern in terms of the velocity component v) are visible in the horizontal velocity field instead of horizontal layers (figure 2*e*). Hence, the weakening of the stable stratification in these regions allows for the existence of vortices associated with strong vertical motions. These regions are separated by thin layers where the stratification is intensified and where vortices are absent. Such a structure with weakly stratified regions of strong turbulence alternating with strongly stratified regions with weak turbulence is reminiscent of the mechanism for the emergence of density layers in stratified turbulence proposed by Phillips (1972) and Posmentier (1977).

Later, b_{rms}/N is again minimum at $t \approx 4000$ (figure 5). There are then layers almost everywhere (figure 4) although they are irregular. By $t \approx 4700$ (figure 5), a new peak of b_{rms}/N is observed and again a region where strong vortices are present can be seen around $z = 15-20$ (figure 2*f*). The vertical gradient of total buoyancy b_t is weakened in this region (not shown).

Finally, we stress that if the simulation is repeated for the same parameters, but with a different occurrence of random noise, the overall characteristics of the different fields at a given time are identical, but they differ locally. In particular, the location of the layers varies, but their number at a given time is similar.

3.2. *Energy analysis*

Figure 7 shows the different terms of the total energy equation:

$$\frac{\mathrm{d}(E_k + E_p)}{\mathrm{d}t} = -\epsilon - \chi + P, \tag{3.3}$$

https://doi.org/10.1017/jfm.2025.10930 Published online by Cambridge University Press

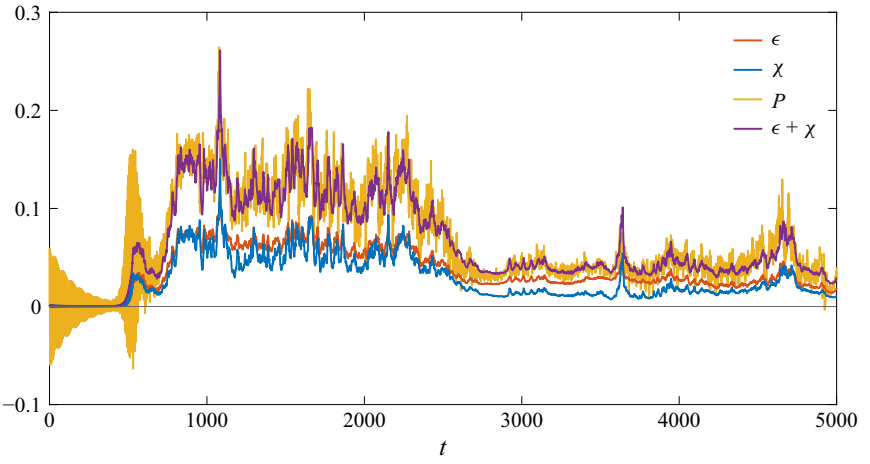


Figure 7. Evolution of the energy dissipations and production as defined in (3.3) for $Re = 8840$, $F_h = 0.4$ and $k_{yf} = k_{zf} = 4k_0$. The different lines correspond to the dissipation of kinetic energy ϵ (red), the dissipation of potential energy χ (blue), the energy provided by the forcing P (yellow) and the total dissipation (purple).

where $E_k = v_{rms}^2/2 + w_{rms}^2/2$, $E_p = b_{rms}^2/(2N^2)$ are the kinetic and potential energies, whereas $\epsilon = \nu\langle \boldsymbol{\nabla u} : \boldsymbol{\nabla u}\rangle_{y,z}$ is the dissipation of kinetic energy, $\chi = \kappa\langle \boldsymbol{\nabla} b^2\rangle_{y,z}/N^2$ the dissipation of potential energy and $P = \langle \boldsymbol{F}.\boldsymbol{u}\rangle_{y,z}$ the energy supplied by the forcing, each quantity being averaged over the domain. The dissipation of kinetic energy (red line) and potential energy (blue line) are of the same order as expected for strongly stratified turbulence (Maffioli *et al.* 2016). The mean mixing efficiency is $\Gamma = \chi/\epsilon \simeq 0.7$ during the statistically steady regime. Such a large value could come from the fact that the scaled buoyancy b/N is larger than the velocity perturbations (figure 5). The total dissipation $\epsilon + \chi$ (purple line) is almost superposed on the energy production rate P (yellow line). This demonstrates that the flow is close to a statistically stationary state in which all the energy injected is dissipated. The rapid fluctuations of P, which are absent in ϵ and χ, are due to conversion between kinetic and potential energies.

We can also distinguish two regimes in the saturation phase (figure 7). For $800 \lesssim t \lesssim 2500$, the energy production rate P is high, while beyond $t \approx 2500$, there is a decrease to a level approximately half of that before. Interestingly, these two time ranges correspond to the regimes of regularly thin alternated layers and of irregular thick layers (figures 2 and 4), respectively.

4. Parametric study

4.1. *Effect of the forcing amplitude*

The amplitude of the forcing q_0 has been varied in the range $0.083 < q_0 < 0.91$ by steps of 0.083 or 0.041 for $N = 1.75$, $\nu = 0.008$ and $k_{yf} = k_{zf} = 4k_0$ (table 1). This corresponds to Froude numbers in the range $0.16 \leqslant F_h \leqslant 0.54$. A similar evolution as for the simulation for $q_0 = 0.5$, presented in the previous section, has been observed for each case, but with some differences. In particular, the transition towards a layered turbulent flow occurs sooner as q_0 increases. Indeed, figure 8 shows that the initial growth rate of the r.m.s. of v (blue circle) and $\langle v\rangle_y$ (green diamonds) increase linearly with q_0. Furthermore, the growth rate of $\langle v\rangle_{y-rms}$ is always twice that of v_{rms}.

https://doi.org/10.1017/jfm.2025.10930 Published online by Cambridge University Press

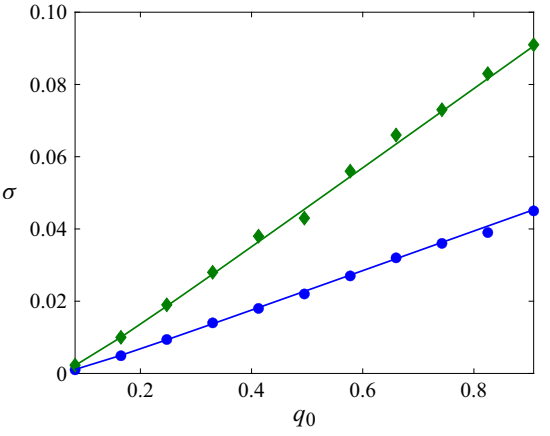


Figure 8. Growth rates of the r.m.s. of the horizontal velocity v (blue circles) and the mean $\langle v\rangle_y$ (green diamonds) as a function of the forcing amplitude q_0 for $N = 1.75$, $\nu = 0.008$ and $k_{yf} = k_{zf} = 4k_0$. The blue and green lines show the growth rate σ and 2σ, respectively, computed from (A9) for each values of q_0.

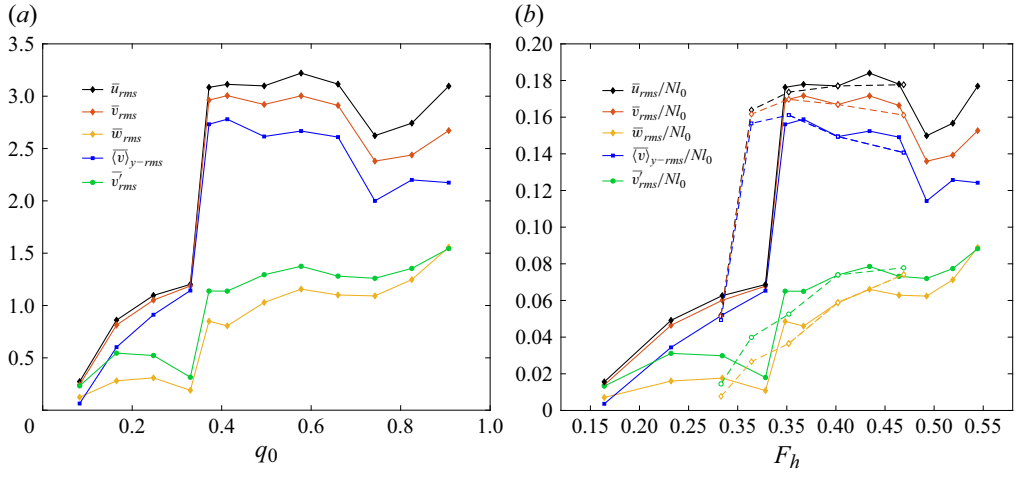


Figure 9. (*a*) Averaged root mean square of the various velocity components as a function of the forcing amplitude q_0 for $N = 1.75$ and $\nu = 0.008$. (*b*) Averaged root mean square of the various velocity components divided by Nl_0 as a function of the Froude number for $\nu = 0.008$. The different lines correspond to $\overline{u}_{rms}$ (black), $\overline{v}_{rms}$ (red), $\overline{w}_{rms}$ (yellow), $\overline{\langle v\rangle}_{y-rms}$ (blue) and $\overline{v'}_{rms}$ (green). In panel (*b*), the solid and dashed lines represent the simulations for variable q_0 for $N = 1.75$ and for variable N for $q_0 = 0.5$, respectively. The forcing wavenumbers are $k_{yf} = k_{zf} = 4k_0$.

In addition, the velocity fluctuations tend to increase with q_0. Figure 9(*a*) shows the root mean square of the total velocity (black line) averaged over a time interval once the flow is statistically stationary,

$$\overline{u}_{rms} = \frac{1}{T}\sum_{t=t_0}^{t_0+T}\sqrt{\langle v^2\rangle_{y,z} + \langle w^2\rangle_{y,z}}, \tag{4.1}$$

where $T = 1000$ and the starting time t_0 is chosen for each q_0 such that the r.m.s. quantities start to be reasonably statistically stationary after this time. However, it should be stressed

https://doi.org/10.1017/jfm.2025.10930 Published online by Cambridge University Press

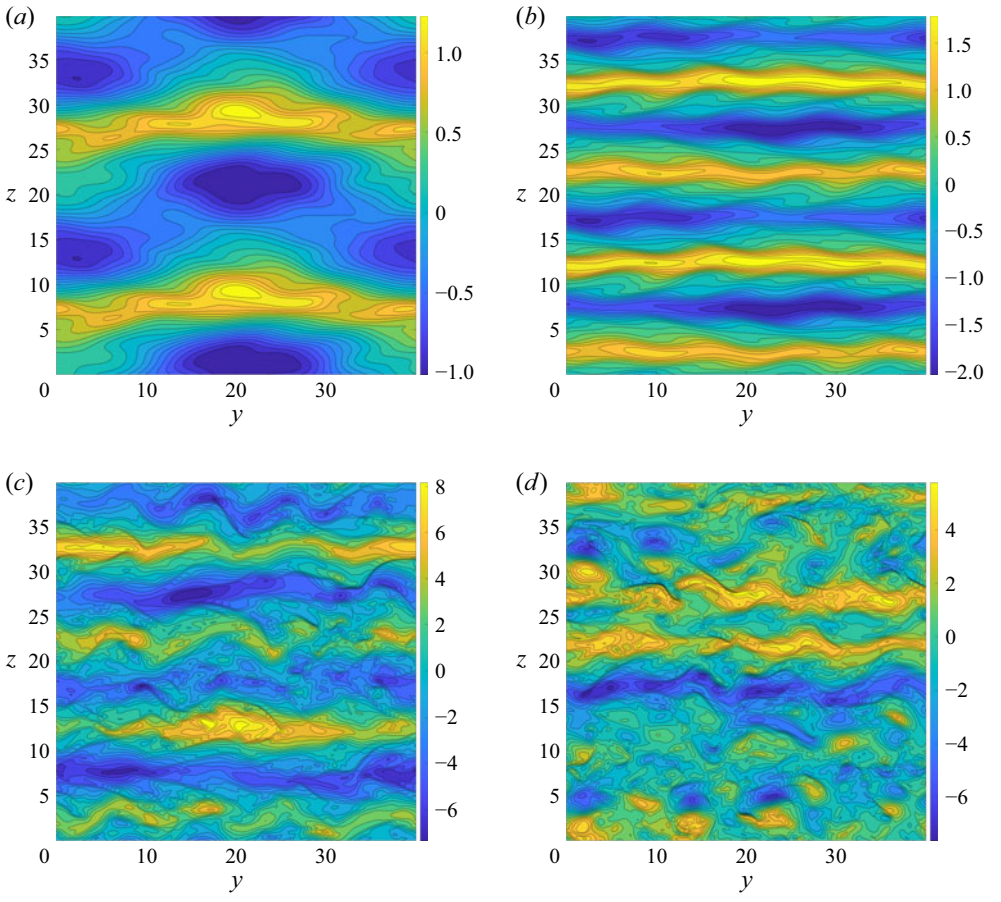


Figure 10. Snapshots of the horizontal velocity field v in the statistically steady regime for various values of q_0: (*a*) $q_0 = 0.17$, $t = 4043$; (*b*) $q_0 = 0.33$, $t = 2471$; (*c*) $q_0 = 0.58$, $t = 2023$; (*d*) $q_0 = 0.74$, $t = 1968$ for $\nu = 0.008$, $N = 1.75$ and $k_{yf} = k_{zf} = 4k_0$. In each case, the instant shown corresponds to the time $t_0 + 1000$.

that, for $q_0 < 0.4$, the r.m.s. can fluctuate largely over a long time scale so that $\overline{u}_{rms}$ depends somewhat on the particular time interval chosen.

We can see that $\overline{u}_{rms}$ first increases continuously and moderately with q_0, and then increases abruptly between $q_0 = 0.33$ and $q_0 = 0.37$ (figure 9*a*). For larger values of q_0, $\overline{u}_{rms}$ remains approximately constant although a small local decrease can be observed around $q_0 \approx 0.8$. The root mean squares of each velocity component, and of $\langle v \rangle_y$ and v' averaged over the same time range are also plotted in figure 9(*a*). The $\overline{v}_{rms}$ and $\langle \overline{v} \rangle_{y-rms}$ follow approximately the same trend as $\overline{u}_{rms}$, whereas the fluctuations $\overline{v}'_{rms}$ and $\overline{w}_{rms}$ vary a little more smoothly.

The horizontal velocity component v is displayed in figure 10 for various values of q_0 at the instant $t = t_0 + T$, i.e. in the statistically steady regime. For low q_0 (figure 10*a*), a mean flow component is present, but the layers tend to exhibit large and smooth variations that travel along the horizontal direction. Figure 10*a* corresponds to a late time $t = 4043$ and there are only four layers. However, eight layers are present at earlier times, like in figure 2. For larger values of the forcing amplitude: $q_0 = 0.33$ (figure 10*b*) and $q_0 = 0.58$ (figure 10*c*), eight regular layers become clearly visible, but they tend to be increasingly more distorted as q_0 increases. We can notice that these layers are located at the same

https://doi.org/10.1017/jfm.2025.10930 Published online by Cambridge University Press

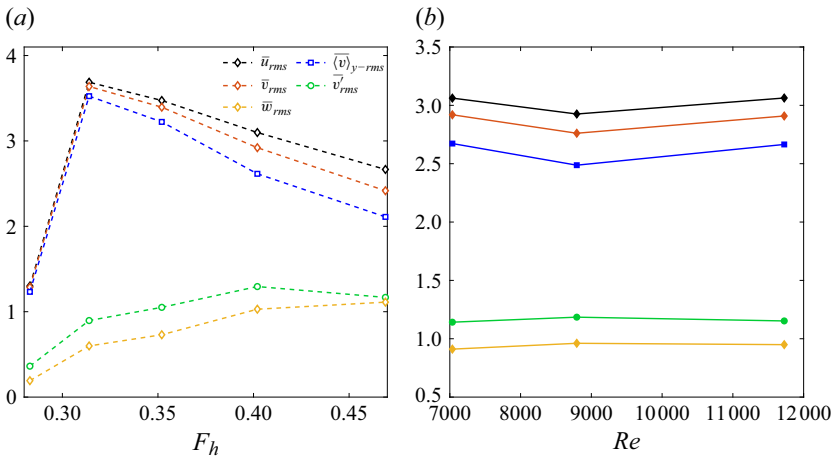


Figure 11. (*a*) Averaged root mean square of the various velocity components as a function of the Froude number F_h for variable N for $q_0 = 0.5$ and $\nu = 0.008$. (*b*) Averaged root mean square of the various velocity components as a function of the Reynolds number Re for variable ν for $q_0 = 0.5$, $N = 1.75$ and $k_{yf} = k_{zf} = 4k_0$. The different lines correspond to $\overline{u}_{rms}$ (black), $\overline{v}_{rms}$ (red), $\overline{w}_{rms}$ (yellow), $\langle\overline{v}\rangle_{y-rms}$ (blue) and $\overline{v'}_{rms}$ (green). The forcing wavenumbers are $k_{yf} = k_{zf} = 4k_0$.

vertical coordinates as for $q_0 = 0.5$, but their sign (i.e. direction of v) is opposite compared with figure 2(*d*). Finally, for $q_0 = 0.74$ (figure 10*d*), the layers are not regularly alternated and there exist regions where vortices are present (lower and upper parts) as for $q_0 = 0.5$ at late time (figure 2*f*). Apart from variations in the number and location of layers, which may depend on the particular time $t_0 + T$ chosen, the main observation in figure 10 is that small-scale turbulent fluctuations increase with q_0, which is observable at any time in the statistically steady regime, as we have already seen in figure 9(*a*).

4.2. *Effects of the Brunt–Väisälä frequency and the viscosity*

The Brunt–Väisälä frequency has been varied in the range $1.5 \leqslant N \leqslant 2.5$ for $q_0 = 0.5$, $\nu = 0.008$ and $k_{yf} = k_{zf} = 4k_0$. The corresponding Froude number lies in the range $0.28 \leqslant F_h \leqslant 0.47$. Figure 11(*a*) shows the root mean square of the various velocity components averaged over the time interval $[t_0, t_0 + T]$ as in figure 9. The average r.m.s. of the mean flow $\langle\overline{v}\rangle_{y-rms}$ increases abruptly and then decreases as the Froude number F_h increases. In contrast, the average r.m.s. of the horizontal velocity fluctuations $\overline{\langle v'\rangle}_{rms}$ and of the vertical velocity $\overline{\langle w'\rangle}_{rms}$ increase weakly with F_h. Hence, $\overline{u}_{rms}$ and $\overline{v}_{rms}$ evolve with F_h similarly as $\overline{\langle v\rangle}_{y-rms}$.

The open symbols with dashed lines in figure 9(*b*) show the same average r.m.s. quantities as in figure 11(*a*), but now non-dimensionalised by Nl_0. We can see that the variations of these non-dimensional r.m.s. are then globally consistent with those when q_0 is varied (full symbols with solid lines).

Finally, figure 11(*b*) shows that the various average r.m.s. quantities are all almost independent of the Reynolds number when the viscosity is varied in the range $0.006 \leqslant \nu \leqslant 0.01$ for $q_0 = 0.5$, $N = 1.75$ and $k_{yf} = k_{zf} = 4k_0$. Altogether, the dependencies of $\overline{u}_{rms}$ (and other r.m.s. quantities) on the control parameters can be therefore written in the non-dimensional form,

$$\frac{\overline{u}_{rms}}{Nl_0} \simeq \mathcal{F}(F_h). \tag{4.2}$$

https://doi.org/10.1017/jfm.2025.10930 Published online by Cambridge University Press

5. Mechanisms of transition and of layer formation

5.1. *Mean flow equation*

As a preliminary step to understand how a mean flow can be generated, it is instructive to consider the mean flow equation,

$$\frac{\partial \langle v \rangle_y}{\partial t} = \mathcal{R} + \frac{1}{Re}\frac{\partial^2 \langle v \rangle_y}{\partial z^2}, \tag{5.1}$$

which can be obtained by applying the mean operator $\langle . \rangle_y$ to the momentum (2.1*a*) in the horizontal direction. The averages of all the other terms of (2.1*a*) vanish due to the periodic boundary conditions. The source of the mean flow is the Reynolds stress divergence given by

$$\mathcal{R} = -\frac{\partial \langle v'w \rangle_y}{\partial z}. \tag{5.2}$$

To see which modes can contribute to $\mathcal{R}$, it is interesting to consider a streamfunction ψ' of the velocity fluctuations (v', w) consisting in the sum of a pair of modes with wavevectors $\boldsymbol{k}_A$ and $\boldsymbol{k}_B$:

$$\psi' = \psi_A(t)e^{\mathrm{i}(k_{yA}y + k_{zA}z)} + \psi_B(t)e^{\mathrm{i}(k_{yB}y + k_{zB}z)} + \text{c.c.}, \tag{5.3}$$

where ψ_A, ψ_B are their amplitudes. This leads to the Reynolds stress divergence:

$$\begin{aligned}\mathcal{R}(\boldsymbol{k}_A, \boldsymbol{k}_B) = (k_{zA}k_{yB} + k_{zB}k_{yA})\Big[&\delta(k_{yA} - k_{yB})(k_{zA} - k_{zB})\left(\mathrm{i}\psi_A\psi_B^* e^{\mathrm{i}(k_{zA}-k_{zB})z} + \text{c.c.}\right)\\ &- \delta(k_{yA} + k_{yB})(k_{zA} + k_{zB})\left(\mathrm{i}\psi_A\psi_B e^{\mathrm{i}(k_{zA}+k_{zB})z} + \text{c.c.}\right)\Big],\end{aligned} \tag{5.4}$$

where δ is the Dirac function. Here and hereinafter, we use the shorthand notation $\mathcal{R}(\boldsymbol{k}_A, \boldsymbol{k}_B) = \mathcal{R}(\boldsymbol{k}_A, \boldsymbol{k}_B, \psi_A, \psi_B)$. As shown by Galmiche *et al.* (2000) for two internal waves, the expression (5.4) shows that the interaction of two modes can contribute to the Reynolds stress divergence, i.e. produce a mean flow, only if they have equal absolute horizontal wavenumbers, $|k_{yA}| = |k_{yB}|$, and different absolute vertical wavenumbers, $|k_{zA}| \neq |k_{zB}|$. This implies the well-known result that the self-interaction of a mode cannot generate a mean flow. In addition, we recover the fact that the modes A, B and the mean flow cannot form an unstable resonant triad since the temporal resonance condition $\omega_A = \omega_B$ and $|k_{yA}| = |k_{yB}|$ imply $|k_{zA}| = |k_{zB}|$ so that $\mathcal{R}(\boldsymbol{k}_A, \boldsymbol{k}_B) = 0$ (Phillips 1968; McEwan *et al.* 1972). These simple conditions are valid at any time and for arbitrary amplitude of the modes. They should be kept in mind in the next section, where we will determine how a mean flow can emerge.

5.2. *Instability mechanism*

To understand the first instability leading to a transition towards turbulence, we now look at the dominant Fourier modes $\hat{v}$ of the horizontal velocity (see (2.8)). Figure 12 first shows the amplitudes of the Fourier modes that are above a threshold in the wavenumbers space (k_y, k_z) at $t = 380$ for $F_h = 0.4$, $Re = 8840$ and $k_{yf} = k_{zf} = 4k_0$. The grid represents the discrete wavenumbers resolved in the numerical simulations, i.e. (nk_0, pk_0), where n and p are integers. Only the quadrant of positive wavenumbers is displayed since the three other quadrants are nearly symmetric and similar. Several modes with an even vertical wavenumber up to $20k_0$ are significant at that time. They are located at $k_z = 4nk_0$ or $k_z = 2 + 4nk_0$, where n is a positive integer, if the horizontal wavenumber k_y is an even or odd number of k_0, respectively. The labels of the modes in figure 12 will be explained later.

https://doi.org/10.1017/jfm.2025.10930 Published online by Cambridge University Press

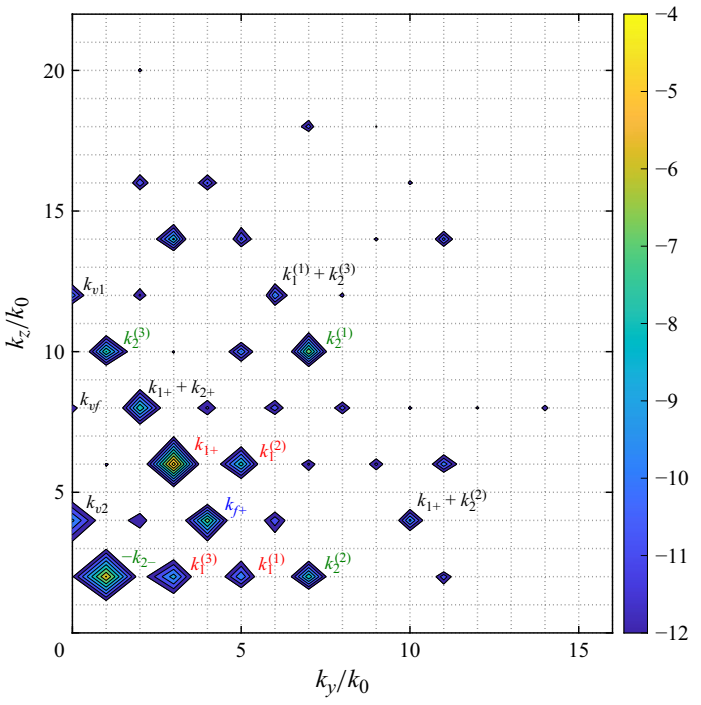


Figure 12. Amplitudes of the Fourier modes $\hat{v}$ of the horizontal velocity at $t = 380$ for $F_h = 0.4$, $Re = 8840$ and $k_{yf} = k_{zf} = 4k_0$. The colour scale is given in natural logarithm. The grid represents the discrete wavenumbers resolved in the numerical simulations. The wavevectors labelled $\boldsymbol{k}_{1+}$, $-\boldsymbol{k}_{2-}$, $\boldsymbol{k}_{f+}$ are the resonant wavevectors, whereas the first non-resonant modes, $\boldsymbol{k}_1^{(i)}$ and $\boldsymbol{k}_2^{(i)}$ with $i = \{1, 2, 3\}$, which are linearly generated by the interactions with the forced wavevectors $\boldsymbol{k}_{f-}$, $-\boldsymbol{k}_{f-}$, $-\boldsymbol{k}_{f+}$, are labelled in red and green, respectively. The wavevectors labelled in black correspond to a sample of modes that are nonlinearly generated.

Figure 13(a) shows the time evolution of all the modes (grey lines) in the ranges: $0 \leqslant k_{yf} \leqslant 12k_0$, $0 \leqslant k_{zf} \leqslant 12k_0$. Like in figure 1, a moving average over a time interval $\Delta t = 5$ has been applied to smooth rapid oscillations. The three dominant modes are highlighted in colour. The mode ($4k_0$,$4k_0$) (blue line) is the one which is directly forced. It initially follows the same evolution as in figure 1(b). The two other modes have wavenumbers $(k_y, k_z) = (3k_0, 6k_0)$ (green line) and $(k_0, 2k_0)$ (orange line). They are initially very small, but they grow exponentially (figure 13a) and become dominant for $t \gtrsim 350$. The three other plots of figure 13 are identical except that different subdominant modes are plotted in colour. They will be explained later.

The origin of this instability can be understood from the resonant interaction theory of weak internal waves (McEwan 1971; McEwan *et al.* 1972; LeBlond & Mysak 1981; Staquet & Sommeria 2002; Dauxois *et al.* 2018). Following this theory, we consider the wavevector $\boldsymbol{k}_{f+} = (k_{yf}, k_{zf})$ of the solution (2.4) at leading order and two linear internal waves with wavevectors $\boldsymbol{k}_{1+}$ and $\boldsymbol{k}_{2+}$, and frequency ω_{1+} and ω_{2+}. They can form a resonant triad when the following conditions are met:

$$\boldsymbol{k}_{1+} = \boldsymbol{k}_{f+} + \boldsymbol{k}_{2+}, \tag{5.5a}$$

$$\omega_{1+} = \omega_{f+} + \omega_{2+}, \tag{5.5b}$$

where ω_{js} for $j = \{1, 2\}$ and $s = \{+, -\}$ are given by the dispersion relation:

$$\omega_{js} = \pm N \frac{k_{yjs}}{\|\boldsymbol{k}_{js}\|}. \tag{5.6}$$

https://doi.org/10.1017/jfm.2025.10930 Published online by Cambridge University Press

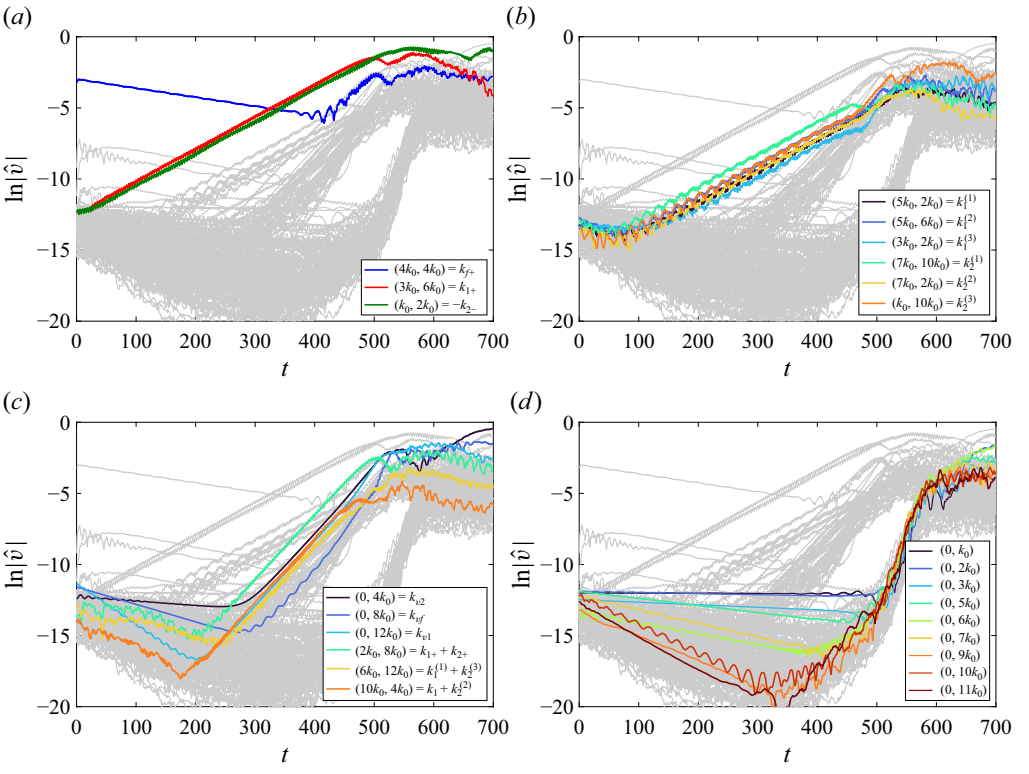


Figure 13. Evolution of the modes in the wavenumber ranges $[0,\ 12k_0] \times [0,\ 12k_0]$ for $F_h = 0.4$, $Re = 8840$ and $k_{yf} = k_{zf} = 4k_0$. The y-axis corresponds to natural logarithm. In each of the four plots, all the modes are plotted in grey lines, but different modes are highlighted in colour. In panel (a), the three dominant modes $\boldsymbol{k}_{1+}$, $\boldsymbol{k}_{2-}$, $\boldsymbol{k}_{f+}$ are displayed in colour. In panel (b), the modes $\boldsymbol{k}_1^{(i)}$ and $\boldsymbol{k}_2^{(i)}$ with $i = \{1,\ 2,\ 3\}$, resulting from the interactions with $\boldsymbol{k}_{f-}$, $-\boldsymbol{k}_{f-}$, $-\boldsymbol{k}_{f+}$, are plotted in colour. In panel (c), the three shear modes $\boldsymbol{k}_{vf}$, $\boldsymbol{k}_{v1}$, $\boldsymbol{k}_{v2}$ and a sample of other modes, labelled in black in figure 12, that grow at a rate 2σ are plotted in colour. In panel (d), the other shear modes are displayed in colour. A moving average over a time interval $\Delta t = 5$ has been applied to filter the oscillations at frequency Ω.

The sign convention chosen in (5.5a) is arbitrary since the amplitudes of any pair of wavevectors $\boldsymbol{k}$ and $-\boldsymbol{k}$ are the complex conjugate of each other so that the fields are real. In contrast with the classical theory of resonant wave interactions, the primary wave will be considered here to be steady, $\omega_{f+} = 0$, since the dominant term of the solution (2.4), i.e. the leading term in q_0 of b, becomes quickly steady (see figure 1a).

After some manipulations, the conditions of spatial and temporal resonances (5.5) can be reduced to

$$k_{z1+} = \frac{k_{zf} k_{y1+}}{2k_{y1+} - k_{yf}}. \tag{5.7}$$

Without loss of generality, we can assume $k_{y1+} > k_{yf}/2$ since the complementary interval simply corresponds to the change $(\boldsymbol{k}_{1+}, \boldsymbol{k}_{2+}) \to (-\boldsymbol{k}_{2+}, -\boldsymbol{k}_{1+})$ in (5.5). The solution (5.7) is shown by a red dashed line in figure 14. In addition, the solid red contour delimits the region where the triad is unstable according to the growth rate (A9) obtained from a multiscale asymptotic analysis for small Froude number F_h and large Reynolds number Re (Appendix). This analysis does not consider only exact resonance but also quasi-resonance, i.e. when (5.5b) is not satisfied exactly, but only with a detuning of

https://doi.org/10.1017/jfm.2025.10930 Published online by Cambridge University Press

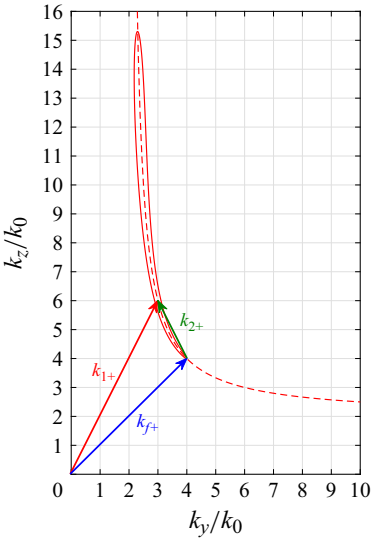


Figure 14. Components of the wavevector $\boldsymbol{k}_{1+}$ (red dashed line) satisfying the resonance conditions (5.5) for $\boldsymbol{k}_{f+} = (4k_0, 4k_0)$. The red solid line delimits the unstable region predicted by (A9) for $q_0 = 0.5$, $\nu = 0.008$ and $N = 1.75$. The grid represents the discrete wavenumbers resolved in the numerical simulations. The coloured vectors represent the unstable triad $(\boldsymbol{k}_{f+}, \boldsymbol{k}_{1+}, \boldsymbol{k}_{2+})$.

order $O(F_h^2)$. This is the reason why the instability band in figure 14 has a finite width around the exact resonance curve. We can see that the sole discrete wavevector resolved in the numerical simulations that is within the unstable region is $\boldsymbol{k}_{1+} = (3k_0, 6k_0)$. Actually, it coincides with the dashed red curve meaning that the resonance is exact. The complementary wavevector of the resonant triad is then $\boldsymbol{k}_{2+} = (-k_0, 2k_0)$, as represented in green in figure 14. The wavevector $\boldsymbol{k}'_{1+} = (6k_0, 3k_0)$ (associated with $\boldsymbol{k}'_{2+} = (2k_0, -k_0)$) lies also on the curve of exact resonance, but it is stable. The stability analysis in the Appendix shows indeed that a necessary condition for instability is that k_{y1+} and k_{y2+} should be of opposite sign. Note that the width and upper k_z limit of the unstable domain depend on the parameters (q_0, ν, N) (see A9).

There is therefore a single unstable triad associated to the wavevector $\boldsymbol{k}_{f+}$:

$$\boldsymbol{k}_{f+} = (4k_0, 4k_0), \quad \boldsymbol{k}_{1+} = (3k_0, 6k_0), \quad \boldsymbol{k}_{2+} = (-k_0, 2k_0). \tag{5.8a}$$

The equivalent triad for the wavevector $\boldsymbol{k}_{f-}$ (see (2.3)) can be simply obtained by the sign change $k_z \to -k_z$:

$$\boldsymbol{k}_{f-} = (4k_0, -4k_0), \quad \boldsymbol{k}_{1-} = (3k_0, -6k_0), \quad \boldsymbol{k}_{2-} = (-k_0, -2k_0). \tag{5.8b}$$

There exist two other triads with opposite wavevectors, but they are linked to their above-mentioned counterparts due to the relation between the amplitudes of $\boldsymbol{k}$ and $-\boldsymbol{k}$ wavevectors. Altogether, these symmetries imply that there is a pair of resonant wavevectors in each quadrant of the wavenumber space (k_y, k_z). This is the reason why we can focus our attention on only the upper right quadrant as done in figures 12 and 13.

The wavevectors $\boldsymbol{k}_{1+}$ and $-\boldsymbol{k}_{2-}$ correspond exactly to the first two Fourier modes that grow exponentially in figure 13(*a*) (green and orange lines). Furthermore, the growth rate computed from the asymptotic formula (A9) in the Appendix is $\sigma_r = 0.0227$ in very good agreement with the slope of 0.023 of the orange and yellow lines in figure 13(*a*).

So far, we have considered only the interaction terms between the forced wavevectors and the perturbations that satisfy the resonance conditions (5.5). However, many other

https://doi.org/10.1017/jfm.2025.10930 Published online by Cambridge University Press

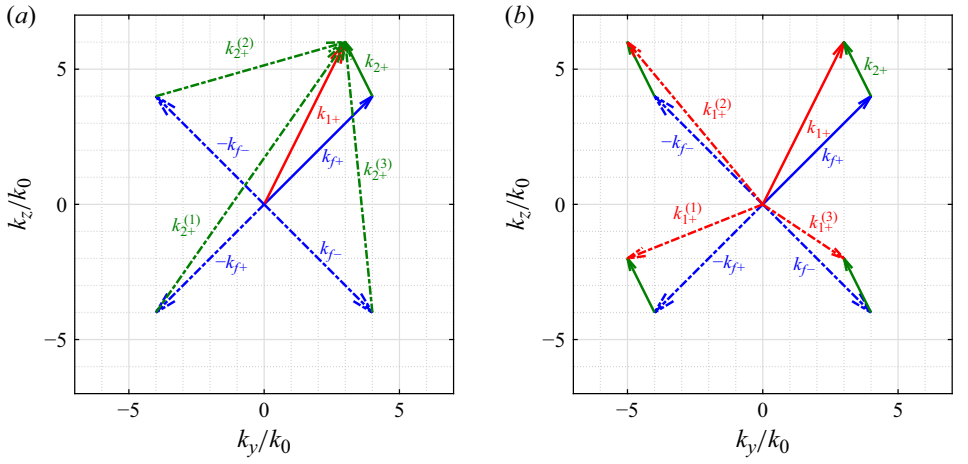


Figure 15. Representation of the wavevectors of the triad with subscript + (solid lines) and of the non-resonant wavevectors (dashed lines) generated by the interaction with the other wavevectors of the base solution $(-\boldsymbol{k}_{f+}, \boldsymbol{k}_{f-}, -\boldsymbol{k}_{f-})$. (*a*) Non-resonant wavevectors $\boldsymbol{k}_{2+}^{(1)}, \boldsymbol{k}_{2+}^{(2)}, \boldsymbol{k}_{2+}^{(3)}$ are indicated by green dashed vectors. (*b*) Non-resonant wavevectors $\boldsymbol{k}_{1+}^{(1)}, \boldsymbol{k}_{1+}^{(2)}, \boldsymbol{k}_{1+}^{(3)}$ are represented by red dashed vectors.

non-resonant modes are also generated as illustrated in figure 15 in the case of the triad with subscript +. The green dashed vectors in figure 15(*a*) represent the non-resonant wavevectors that are generated by the interactions of $\boldsymbol{k}_{1+}$ with $(-\boldsymbol{k}_{f+}, -\boldsymbol{k}_{f-}, \boldsymbol{k}_{f-})$:

$$\boldsymbol{k}_{2+}^{(1)} \equiv \boldsymbol{k}_{1+} + \boldsymbol{k}_{f+} = (7k_0, 10k_0), \quad \boldsymbol{k}_{2+}^{(2)} \equiv \boldsymbol{k}_{1+} + \boldsymbol{k}_{f-} = (7k_0, 2k_0),$$
$$\boldsymbol{k}_{2+}^{(3)} \equiv \boldsymbol{k}_{1+} - \boldsymbol{k}_{f-} = (-k_0, 10k_0), \tag{5.9}$$

respectively. Similarly, the red dashed vectors in figure 15(*b*) show the non-resonant wavevectors produced by the interactions between $\boldsymbol{k}_{2+}$ and $(-\boldsymbol{k}_{f+}, -\boldsymbol{k}_{f-}, \boldsymbol{k}_{f-})$:

$$\boldsymbol{k}_{1+}^{(1)} \equiv \boldsymbol{k}_{2+} - \boldsymbol{k}_{f+} = (-5k_0, -2k_0), \quad \boldsymbol{k}_{1+}^{(2)} \equiv \boldsymbol{k}_{2+} - \boldsymbol{k}_{f-} = (-5k_0, 6k_0),$$
$$\boldsymbol{k}_{1+}^{(3)} \equiv \boldsymbol{k}_{2+} + \boldsymbol{k}_{f-} = (3k_0, -2k_0), \tag{5.10}$$

respectively.

The same occurs for the triad with subscript − (5.8*b*) and those with opposite wavevectors. Hence, like for the resonant wavevectors $\boldsymbol{k}_{1+}$ and $\boldsymbol{k}_{2+}$, any of the non-resonant wavevectors (5.9) and (5.10) has symmetric counterparts in the three other quadrants. In figure 12 showing only the upper right quadrant of the wavenumber space, the corresponding wavevectors are labelled $\boldsymbol{k}_1^{(1)}, \boldsymbol{k}_1^{(2)}, \boldsymbol{k}_1^{(3)}, \boldsymbol{k}_2^{(1)}, \boldsymbol{k}_2^{(2)}, \boldsymbol{k}_2^{(3)}$ i.e. the sign and subscripts, + or −, are omitted to simplify the notation. The evolutions of their amplitudes are highlighted in figure 13(*b*). Even if their amplitudes are lower than those of the resonant modes, they all grow exponentially at rate σ like the resonant modes. Indeed, since these non-resonant modes are driven by the interaction between the resonant modes $\boldsymbol{k}_{1s}$, $\boldsymbol{k}_{2s}$ with $s = \{+, -\}$ and the forced wavevectors, they should grow at the same rate as the resonant modes. In addition, their frequency is not the natural one, but a forced one: i.e. the same as the wavevectors $\boldsymbol{k}_{1s}$ and $\boldsymbol{k}_{2s}$, i.e. $\pm\omega \equiv \omega_{1s} = \omega_{2s}$ with $s = \{+, -\}$.

Among these eight modes generated by each triad, it is easy to see that some of them have the same horizontal wavenumber, but different vertical wavenumbers. This is the condition for their quadratic interactions to generate shear modes, or equivalently, to contribute to the Reynolds stress divergence (5.4). For example, we see in figure 15(*a*)

https://doi.org/10.1017/jfm.2025.10930 Published online by Cambridge University Press

that the horizontal components of $\boldsymbol{k}_{2+} = (-k_0, 2k_0)$ and $\boldsymbol{k}^{(3)}_{2+} = (-k_0, 10k_0)$ are equal by construction. Hence, the quadratic interactions between $\boldsymbol{k}_{2+}$ and $\boldsymbol{k}^{(3)}_{2+}$, or between $\boldsymbol{k}_{2-}$ and $\boldsymbol{k}^{(3)}_{2+}$, will generate the shear modes

$$\boldsymbol{k}_{vf} \equiv \boldsymbol{k}^{(3)}_{2+} - \boldsymbol{k}_{2+} = \boldsymbol{k}_{f+} - \boldsymbol{k}_{f-} = (0, 2k_{zf}) = (0, 8k_0), \tag{5.11}$$

$$\boldsymbol{k}_{v1} \equiv \boldsymbol{k}^{(3)}_{2+} - \boldsymbol{k}_{2-} = \boldsymbol{k}_{1+} - \boldsymbol{k}_{1-} = (0, 2k_{z1+}) = (0, 12k_0). \tag{5.12}$$

The interactions between $\boldsymbol{k}^{(1)}_{2+}$ and $\boldsymbol{k}^{(2)}_{2+}$ in figure 15(*a*), or between $\boldsymbol{k}^{(1)}_{2+}$ and $\boldsymbol{k}^{(2)}_{2-}$, will produce the same shear modes. Similar considerations in figure 15(*b*) show that the interactions of $\boldsymbol{k}_{1+}$ with $\boldsymbol{k}^{(3)}_{1+}$, $\boldsymbol{k}^{(1)}_{1+}$ with $\boldsymbol{k}^{(2)}_{1+}$, $\boldsymbol{k}_{1-}$ with $\boldsymbol{k}^{(3)}_{1+}$ or $\boldsymbol{k}^{(1)}_{1+}$ with $\boldsymbol{k}^{(2)}_{1-}$ will produce the shear modes $\boldsymbol{k}_{vf}$ and

$$\boldsymbol{k}_{v2} \equiv \boldsymbol{k}^{(3)}_{1+} - \boldsymbol{k}_{1-} = \boldsymbol{k}_{2+} - \boldsymbol{k}_{2-} = (0, 2k_{z2+}) = (0, 4k_0). \tag{5.13}$$

Interchanging the subscripts + an − in the above-mentioned relations leads simply to a sign change. The growth rate of these three shear modes is 2σ and their frequencies are $[-2\omega, 0, 2\omega]$ since they result from a quadratic interaction between modes growing at rate σ with frequency $\pm\omega$. However, the forced response should be highest at zero frequency since this is the natural frequency of shear modes.

The generation of the three shear modes, $(\boldsymbol{k}_{vf}, \boldsymbol{k}_{v1}, \boldsymbol{k}_{v2})$, can be also interpreted in the framework of the quartet resonant mechanism (Newell 1969; Smith & Waleffe 1999). For example, the forced wavevector $\boldsymbol{k}_{f+}$ can be written in terms of its symmetric counterpart with respect to the horizontal axis, $\boldsymbol{k}_{f-}$, and the shear mode $\boldsymbol{k}_{vf}$: $\boldsymbol{k}_{f+} = \boldsymbol{k}_{f-} + \boldsymbol{k}_{vf}$. Hence, the resonance conditions (5.5) can be rewritten in terms of a quartet resonance:

$$\boldsymbol{k}_{1+} = \boldsymbol{k}_{f-} + \boldsymbol{k}_{vf} + \boldsymbol{k}_{2+}, \tag{5.14a}$$

$$\omega_{1+} = \omega_{f-} + \omega_{vf} + \omega_{2+}, \tag{5.14b}$$

where $\omega_{vf} = 0$. A similar substitution with the symmetric with respect to the horizontal could be applied to the two other wavevectors, i.e. $\boldsymbol{k}_{1+} = \boldsymbol{k}_{1-} + \boldsymbol{k}_{v1}$ or $\boldsymbol{k}_{2+} = \boldsymbol{k}_{2-} + \boldsymbol{k}_{v2}$. Then, (5.5) can be also rewritten in terms of a quartet resonance for these two cases.

The evolutions of the shear modes $\boldsymbol{k}_{v2} = (0, 4k_0)$, $\boldsymbol{k}_{vf} = (0, 8k_0)$ and $\boldsymbol{k}_{v1} = (0, 12k_0)$ are highlighted in colour in figure 13(*c*), whereas all the other shear modes $(0, k_z)$ in the band $0 \leqslant k_z \leqslant 12k_0$ are displayed in colour in figure 13(*d*). We can see that the three shear modes $\boldsymbol{k}_{v2}$, $\boldsymbol{k}_{vf}$ and $\boldsymbol{k}_{v1}$ grow exponentially at the rate 2σ as expected from the above-mentioned reasoning. They start to be amplified only after $t \gtrsim 300$ clearly showing that they are a by-product of the triadic instabilities. This explains why the r.m.s. of $\langle v \rangle_y$ grows at a rate twice the r.m.s. of v (inset of figure 5). In contrast, the other shear modes grow only later, $t \gtrsim 400$, at a different growth rate (figure 13*d*). Figure 13(*c*) shows also the evolutions of a sample of other significant modes labelled in black in figure 12 that grow at rate 2σ.

More generally, all the modes with wavenumbers such that $(k_y, k_z) = ((2n+1)k_0, (4p+2)k_0)$, where n and p are integers, grow with a growth rate σ. Indeed, these wavevectors correspond to q successive interactions of $\boldsymbol{k}_{2+}$ with the forced wavevectors, giving $(k_y, k_z) = \boldsymbol{k}_{2+} + 4qk_0(\pm 1, \pm 1)$. In contrast, the modes such that $(k_y = 2nk_0$, $k_z = 4pk_0)$ grow at rate 2σ. These modes are generated by one interaction between $\boldsymbol{k}_{1+}$ and $\boldsymbol{k}_{2+}$ followed by q successive interactions with the forced wavevectors, yielding $(k_y, k_z) = \boldsymbol{k}_{1+} + \boldsymbol{k}_{2+} + 4qk_0(\pm 1, \pm 1)$.

The other modes, i.e. those with an odd vertical wavenumber and those with $(k_y, k_z) = ((2n+1)k_0, 4pk_0)$ or $(k_y, k_z) = (2nk_0, (4p+2)k_0)$ grow only later at a different growth

https://doi.org/10.1017/jfm.2025.10930 Published online by Cambridge University Press

rate, probably due to a secondary triadic instability of modes amplified by the first triadic instability. The shear modes plotted in figure 13(*d*) belong to this family.

In summary, triadic instabilities with the four forced wavevectors $\pm\boldsymbol{k}_{f+}$, $\pm\boldsymbol{k}_{f-}$ of the base solution (2.4) lead first to the exponential amplification of the internal waves with wavevector $\pm\boldsymbol{k}_{1+}$, $\pm\boldsymbol{k}_{1-}$ and $\pm\boldsymbol{k}_{2+}$, $\pm\boldsymbol{k}_{2-}$. The quadratic interactions of these resonant waves with the forced wavevectors drive also the growth at the same rate of several non-resonant modes: $\pm\boldsymbol{k}^{(i)}_{j+}$, $\pm\boldsymbol{k}^{(i)}_{j-}$ for $i=\{1,2,3\}$ and $j=\{1,2\}$. These are not internal waves since their frequency is the same as the resonant waves. Then, the quadratic interactions between all these modes further generate many other modes growing at a double growth rate. Among them, we have shown that there are the shear modes: $\boldsymbol{k}_{vf}=(0,2k_{zf})$, $\boldsymbol{k}_{v1}=(0,2k_{z1+})$ and $\boldsymbol{k}_{v2}=(0,2k_{z2+})$.

We emphasise that this scenario is observed whatever the amplitude of the forcing q_0 in the range investigated. In particular, the asymptotic growth rate (A9) (blue line in figure 8) is in excellent agreement with the growth rate of v_{rms} for all the values of q_0 investigated (blue circles). Similarly, the growth rate of $\langle v\rangle_{y-rms}$ (green diamonds in figure 8) corresponds always to twice the asymptotic growth rate (A9) (green line).

5.3. *Reynolds stress*

In the previous section, we have shown that the pairs of wavevectors $(\boldsymbol{k}_{1s},\boldsymbol{k}^{(3)}_{1r})$, $(\boldsymbol{k}_{2s},\boldsymbol{k}^{(3)}_{2r})$, $(\boldsymbol{k}^{(1)}_{1s},\boldsymbol{k}^{(2)}_{1r})$ or $(\boldsymbol{k}^{(1)}_{2s},\boldsymbol{k}^{(2)}_{2r})$, where s,r stand for any pair among the labels $\{+,-\}$, have the same horizontal wavenumber but different vertical wavenumbers. Therefore, their interaction can contribute to the Reynolds stress divergence (5.2) and be responsible for the generation of the mean flow. Among these pairs of modes, the first two are expected to be dominant initially since they each involve one resonant wavevector, $\boldsymbol{k}_{1s}$ or $\boldsymbol{k}_{2s}$, whose amplitudes are larger than those of the non-resonant wavevectors $\boldsymbol{k}^{(i)}_{1s}$, $\boldsymbol{k}^{(i)}_{2s}$, for $s=\{+,-\}$ and $i=\{1,2,3\}$. Hence, we have computed the Reynolds stress divergence by taking into account only the former pairs of modes. More precisely, the total Reynolds stress $\mathcal{R}$ is approximated as the sum of their individual contributions obtained with (5.4):

$$\begin{aligned}\mathcal{R}=&\,\mathcal{R}\big(\boldsymbol{k}_{1+},\boldsymbol{k}^{(3)}_{1+}\big)+\mathcal{R}\big(\boldsymbol{k}_{1+},\boldsymbol{k}^{(3)}_{1-}\big)+\mathcal{R}\big(\boldsymbol{k}_{1-},\boldsymbol{k}^{(3)}_{1-}\big)+\mathcal{R}\big(\boldsymbol{k}_{1-},\boldsymbol{k}^{(3)}_{1+}\big)\\&+\mathcal{R}\big(\boldsymbol{k}_{2+},\boldsymbol{k}^{(3)}_{2+}\big)+\mathcal{R}\big(\boldsymbol{k}_{2+},\boldsymbol{k}^{(3)}_{2-}\big)+\mathcal{R}\big(\boldsymbol{k}_{2-},\boldsymbol{k}^{(3)}_{2-}\big)+\mathcal{R}\big(\boldsymbol{k}_{2-},\boldsymbol{k}^{(3)}_{2+}\big).\end{aligned}\tag{5.15}$$

Using the mode amplitudes extracted from the simulations, the value of $\mathcal{R}$ predicted by (5.15) has then been compared with the Reynolds stress divergence computed from the full velocity fields with (5.2).

An excellent agreement has been observed in the period of pure exponential growth of the resonant and non-resonant modes, i.e. for $t\leqslant 420$ (see figure 16*a* for $t=380$), confirming the reasoning carried out in § 5.2. However, later on (figure 16*b*), the approximation (5.15) no longer agrees with the Reynolds stress divergence computed directly from the DNS because many other modes than considered in (5.15) contribute significantly to $\mathcal{R}$.

6. Effect of the wavenumbers of the forcing

So far, the wavenumbers of the forcing were fixed to $(k_{yf},k_{zf})=(4k_0,4k_0)$. Here, we now present four simulations with the forcing (2.2) with different forcing wavenumbers: $(k_{yf},k_{zf})=(3k_0,3k_0)$, $(k_{yf},k_{zf})=(4k_0,3k_0)$, $(k_{yf},k_{zf})=(5k_0,4k_0)$ and $(k_{yf},k_{zf})=(4k_0,5k_0)$ for $q_0=0.5$, $N=1.75$ and $\nu=0.008$. These four examples are typical of

https://doi.org/10.1017/jfm.2025.10930 Published online by Cambridge University Press

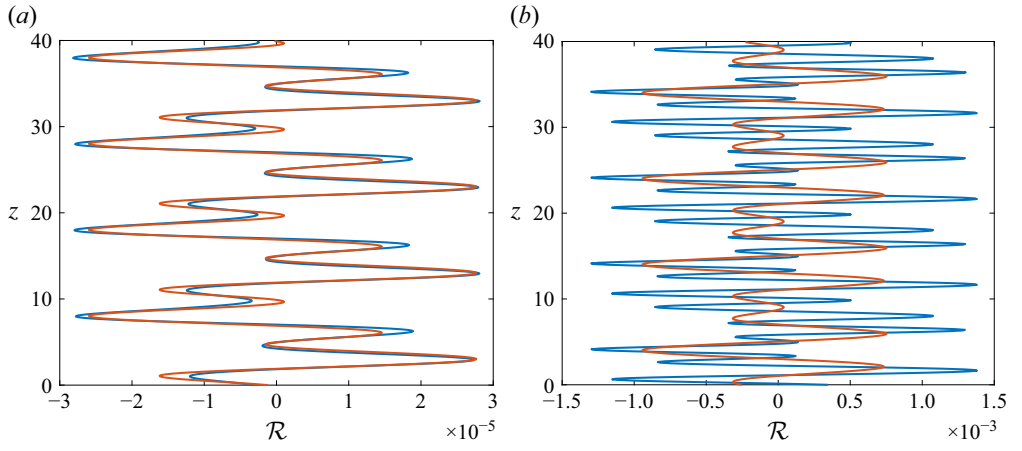


Figure 16. Reynolds stress divergence $\mathcal{R}$ at times (*a*) $t = 380$ and (*b*) $t = 460$ for $Re = 8840$, $F_h = 0.4$ and $k_{yf} = k_{zf} = 4k_0$. The blue line represents $\mathcal{R}$ determined from (5.2), while the orange line corresponds to $\mathcal{R}$ computed with the approximation (5.15).

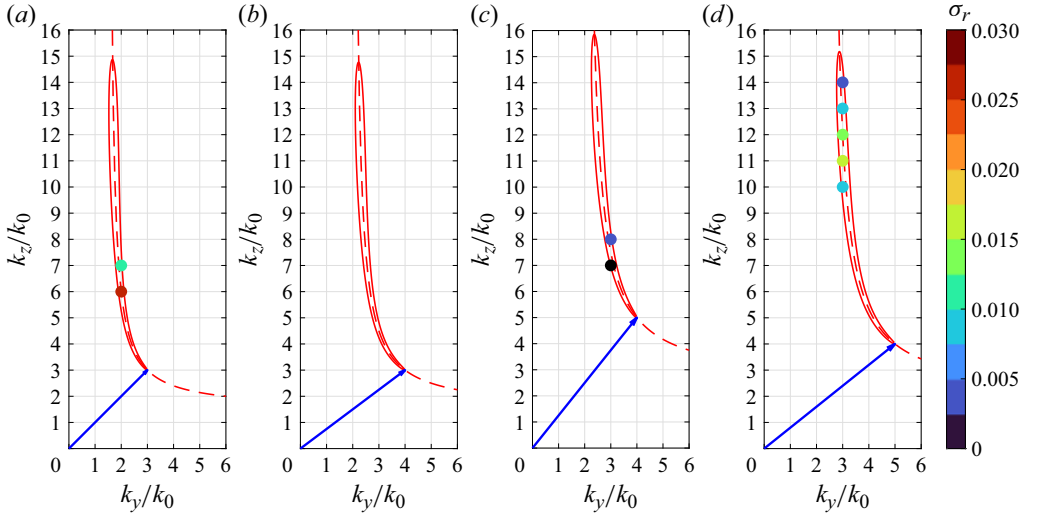


Figure 17. Wavevector $\boldsymbol{k}_{1+}$ satisfying the resonance conditions (5.5) (red dashed line) for (*a*) $\boldsymbol{k}_{f+} = (3k_0, 3k_0)$, (*b*) $\boldsymbol{k}_{f+} = (4k_0, 3k_0)$, (*c*) $\boldsymbol{k}_{f+} = (4k_0, 5k_0)$ and (*d*) $\boldsymbol{k}_{f+} = (5k_0, 4k_0)$ for $q_0 = 0.5$, $\nu = 0.008$, $N = 1.75$. The red solid line delimits the unstable region according to (A9). The blue vector represents the forced wavevector $\boldsymbol{k}_{f+}$. The grid represents the discrete wavenumbers resolved in the numerical simulations. Those that are unstable are highlighted by a circle whose colour indicates the growth rate level (colourbar).

the different behaviours that have been observed in a series of simulations performed systematically in the wavenumber ranges $2k_0 \leqslant k_{yf} \leqslant 5k_0$, $2k_0 \leqslant k_{zf} \leqslant 5k_0$.

Figure 17 first displays the wavevector $\boldsymbol{k}_{1+}$ (red dashed line) satisfying the resonance condition (5.5) for each forcing wavevector $\boldsymbol{k}_{f+}$. As in figure 14, the red solid contour delimits the unstable region according to (A9). The unstable discrete wavenumbers are highlighted by filled circles whose colour indicates the growth rate value (colourbar). For $\boldsymbol{k}_{f+} = (3k_0, 3k_0)$ (figure 17*a*), the wavevector $\boldsymbol{k}_{1+} = (2k_0, 6k_0)$ (red symbol) satisfies exactly the resonance condition and is unstable. The wavevector $\boldsymbol{k}_{1+} = (2k_0, 7k_0)$ (green symbol) is also weakly unstable, but it is only quasi-resonant, i.e. it is inside the unstable

https://doi.org/10.1017/jfm.2025.10930 Published online by Cambridge University Press

band without lying on the curve of exact resonance. For $\boldsymbol{k}_{f+} = (4k_0, 3k_0)$ (figure 17*b*), none of the discrete wavenumbers are unstable.

For $\boldsymbol{k}_{f+} = (4k_0, 5k_0)$ (figure 17*c*), none of the discrete wavenumbers are exactly resonant but there exists two wavevectors that are quasi-resonant: $\boldsymbol{k}_{1+} = (3k_0, 7k_0)$ (dark blue symbol) and $\boldsymbol{k}_{1+} = (3k_0, 8k_0)$ (blue symbol), although the former is only weakly unstable.

Finally, for $\boldsymbol{k}_{f+} = (5k_0, 4k_0)$ (figure 17*d*), there is one unstable exact resonance for $\boldsymbol{k}_{1+} = (3k_0, 12k_0)$ and four unstable quasi-resonance for wavevectors with the horizontal wavenumber $k_{y1+} = 3k_0$ and various vertical wavenumbers in the range $10k_0 \leqslant k_{z1+} \leqslant 14k_0$. Among all these unstable modes, $\boldsymbol{k}_{1+} = (3k_0, 11k_0)$ is dominant, whereas $\boldsymbol{k}_{1+} = (3k_0, 12k_0)$ is slightly subdominant despite it being an exact resonance. The three other wavevectors are somewhat less unstable.

We emphasise that the results in figure 17 refer to the amplitude of the forcing $q_0 = 0.5$. If q_0 were varied, quasi-resonant wavevectors could appear or disappear, because the width of the unstable region around the exact resonance curve increases with the amplitude of the forced solution (2.4) (see (A9)). Thus, quasi-resonant wavevectors should also appear in figure 17(*b*) if q_0 were increased beyond a critical value. Conversely, the quasi-resonant wavevectors in figure 17(*c*) should disappear if q_0 were sufficiently decreased. In contrast, the exact resonances are expected to be less sensitive to variations in q_0.

Figure 18 displays the space–time diagram of the mean horizontal flow $\langle v \rangle_y(z, t)$ for the three unstable cases. When $(k_{yf}, k_{zf}) = (4k_0, 3k_0)$ (not shown), the flow simply evolves according to the solution (2.4) and there are no transition to turbulence and emergence of mean horizontal flows in agreement with the absence of triadic instability (figure 17*b*).

We see that for $(k_{yf}, k_{zf}) = (3k_0, 3k_0)$ (figure 18*a*) and $(k_{yf}, k_{zf}) = (4k_0, 5k_0)$ (figure 18*b*), i.e. when a single pair of resonant modes is dominant, the magnitude of the mean flow and the layer dynamics resemble those for $(k_{yf}, k_{zf}) = (4k_0, 4k_0)$ (figure 4). In contrast, for $(k_{yf}, k_{zf}) = (5k_0, 4k_0)$, the mean flow is much less prominent and the layers tend to fade away after their onset. For the latter case, figure 19 further shows that the root mean square of the mean horizontal flow is smaller than that of the fluctuation v'_{rms} in contrast to figure 5.

The time evolution of all the modes have also been investigated for each case. For $(k_{yf}, k_{zf}) = (3k_0, 3k_0)$ and $(k_{yf}, k_{zf}) = (4k_0, 5k_0)$, i.e. when there is a single pair of dominant resonant wavevectors, the dynamics is very similar to the case $(k_{yf}, k_{zf}) = (4k_0, 4k_0)$, and the emerging shear modes have been observed to be $\boldsymbol{k}_{vf} = (0, 2k_{zf})$, $\boldsymbol{k}_{v1} = (0, 2k_{z1+})$ and $\boldsymbol{k}_{v2} = (0, 2k_{z2+})$ for both cases in agreement with § 5.2. These two cases are therefore not shown. In contrast, for $(k_{yf}, k_{zf}) = (5k_0, 4k_0)$, the dynamics differs because there exist two pairs of dominant resonant modes: $\boldsymbol{k}_{1+} = (3k_0, 11k_0)$, $\boldsymbol{k}_{2+} = (-2k_0, 7k_0)$ and $\boldsymbol{k}_{1+} = (3k_0, 12k_0)$, $\boldsymbol{k}_{2+} = (-2k_0, 8k_0)$. As seen in figure 20(*a*), these four modes grow approximately at the same rate in agreement with the asymptotic stability analysis (figure 17*d*). According to (5.10) and (5.9), the six non-resonant modes generated by the first triad are

$$\begin{aligned} &\boldsymbol{k}^{(1)}_{1+} = (-7k_0, 3k_0), \quad \boldsymbol{k}^{(2)}_{1+} = (-7k_0, 11k_0), \quad \boldsymbol{k}^{(3)}_{1+} = (3k_0, 3k_0), \\ &\boldsymbol{k}^{(1)}_{2+} = (8k_0, 15k_0), \quad \boldsymbol{k}^{(2)}_{2+} = (8k_0, 7k_0), \quad \boldsymbol{k}^{(3)}_{2+} = (-2k_0, 15k_0), \end{aligned} \tag{6.1}$$

while for the second one, they are

$$\begin{aligned} &\boldsymbol{k}^{(1)}_{1+} = (-7k_0, 4k_0), \quad \boldsymbol{k}^{(2)}_{1+} = (-7k_0, 12k_0), \quad \boldsymbol{k}^{(3)}_{1+} = (3k_0, 4k_0), \\ &\boldsymbol{k}^{(1)}_{2+} = (8k_0, 16k_0), \quad \boldsymbol{k}^{(2)}_{2+} = (8k_0, 8k_0), \quad \boldsymbol{k}^{(3)}_{2+} = (-2k_0, 16k_0). \end{aligned} \tag{6.2}$$

https://doi.org/10.1017/jfm.2025.10930 Published online by Cambridge University Press

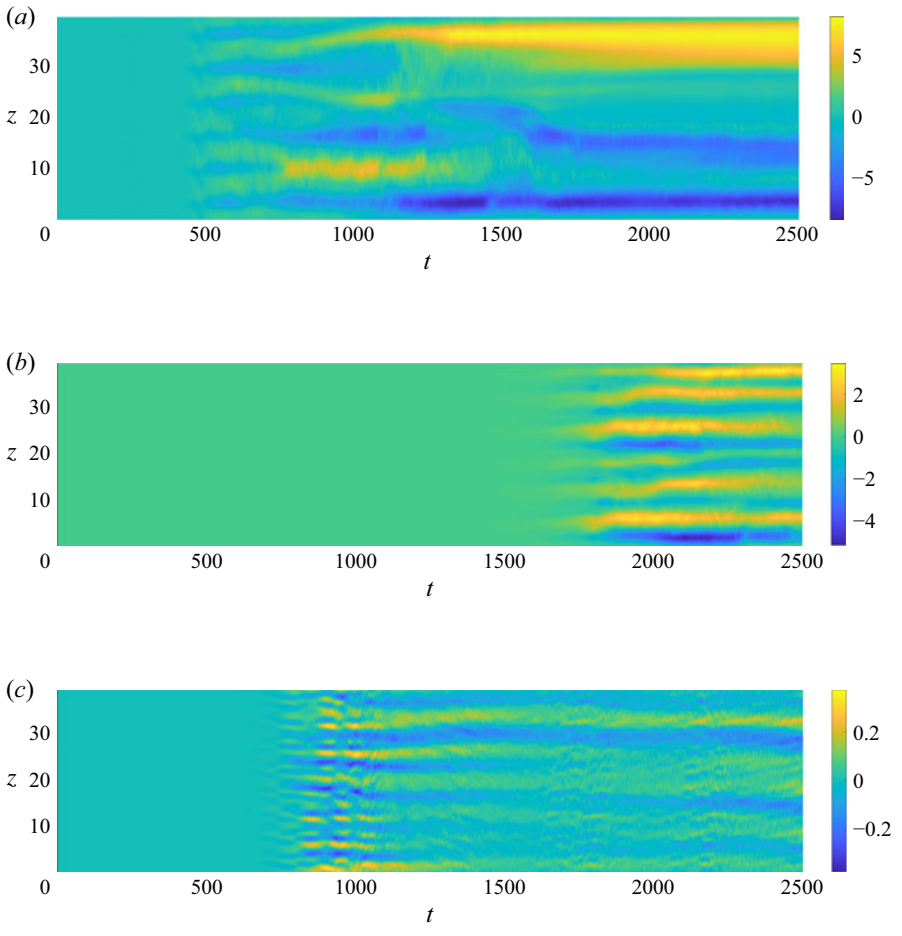


Figure 18. Space–time diagrams of the horizontal mean flow $\langle v\rangle_y(z,t)$ for (a) $(k_{yf}, k_{zf}) = (3k_0, 3k_0)$, (b) $(k_{yf}, k_{zf}) = (4k_0, 5k_0)$ and (c) $(k_{yf}, k_{zf}) = (5k_0, 4k_0)$ for $q_0 = 0.5$, $\nu = 0.008$, $N = 1.75$.

The shear modes that are generated independently by each of the two triads are $\boldsymbol{k}_{vf} = (0, 8k_0)$, $\boldsymbol{k}_{v1} = (0, 22k_0)$, $\boldsymbol{k}_{v2} = (0, 14k_0)$ and $\boldsymbol{k}_{vf} = (0, 8k_0)$, $\boldsymbol{k}_{v1} = (0, 16k_0)$, $\boldsymbol{k}_{v2} = (0, 24k_0)$, respectively. They are highlighted in colour in figure 20(a).

However, the mutual interactions between the resonant and non-resonant modes of the two triads offer the possibility to generate several additional shear modes since they have the same horizontal wavenumber but different vertical wavenumbers. The additional shear modes that can be generated are $(0, k_0)$, $(0, 7k_0)$, $(0, 9k_0)$, $(0, 15k_0)$, $(0, 23k_0)$ in the wavenumber range $0 \leqslant k_z \leqslant 24k_0$. As seen in figure 20$(a)$, these shear modes grow approximately at the same growth rate and their amplitudes are as important as the previous ones. The other shear modes in the band $0 < k_z \leqslant 24k_0$ are plotted in colour in figure 20(b). They start to grow slightly later than those highlighted in figure 20(a). However, the separation between the two groups of shear modes is less clear than previously because some of the shear modes in the second group are generated by non-resonant modes forced by the three other subdominant triads (figure 17d).

Although there are more ways to generate shear modes when there are several triadic instabilities with comparable strength, the amplitude of the mean flow in the statistically steady regime turns out to be lower for $(k_{yf}, k_{zf}) = (5k_0, 4k_0)$ than when there is a single

https://doi.org/10.1017/jfm.2025.10930 Published online by Cambridge University Press

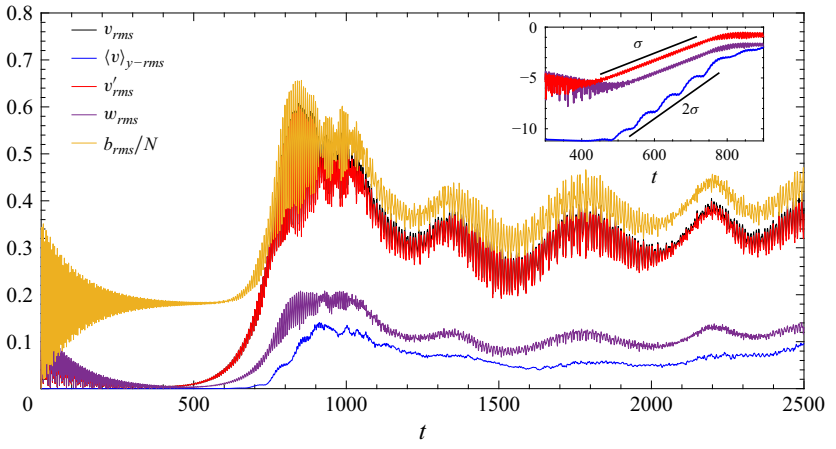


Figure 19. Temporal evolution of the root mean square of the total horizontal velocity v, the mean $\langle v\rangle_y$, the fluctuations v', the vertical velocity w and the scaled buoyancy b/N for $(k_{yf}, k_{zf}) = (5k_0, 4k_0)$ for $F_h = 0.4$ and $Re = 5660$. The inset shows a close-up view of the curves of $\langle v\rangle_{y-rms}$, v'_{rms} and w_{rms} plotted in natural logarithm coordinate.

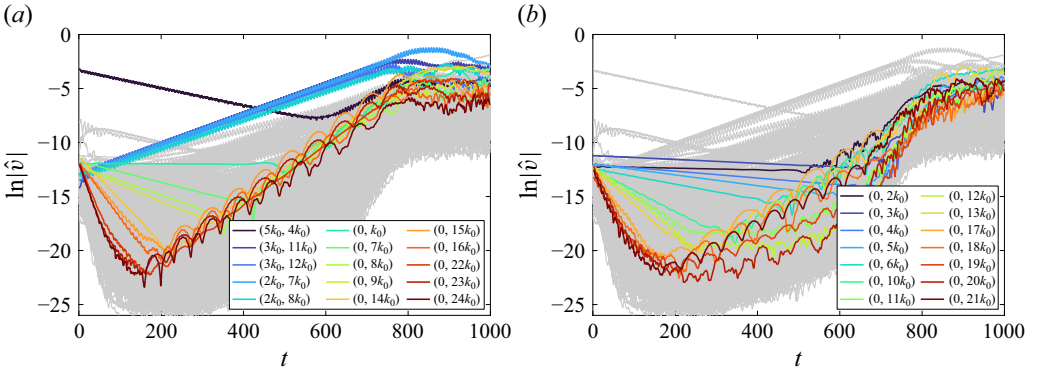


Figure 20. Evolution of the modes (grey lines) in the wavenumbers ranges [0,24k_0]x[0,24k_0] for $(k_{yf}, k_{zf}) = (5k_0, 4k_0)$ for $F_h = 0.4$, $Re = 5660$. In panel (*a*), the forced mode, the two dominant pairs of resonant modes and the resulting shear modes are plotted in colour. In panel (*b*), all the other shear modes $(0, k_z)$ in the band $0 < k_z \leqslant 24k_0$ are highlighted in colour. The y-axis corresponds to natural logarithm. A moving average over a time interval $\Delta t = 5$ has been applied to filter rapid oscillations.

dominant triadic instability. The understanding of this paradoxical effect is left for future studies.

7. Forcing with a single pair of wavenumber

In the previous sections, we have seen that a vertically sheared horizontal mean flow can be generated by the quadratic interactions between two modes that are driven by two different triads that are symmetric with respect to the horizontal. This is possible since the forcing (2.2) contains symmetric wavevectors $\pm\boldsymbol{k}_{f+}$ and $\pm\boldsymbol{k}_{f-}$.

The next question is what happens if the forcing does not contain wavevectors symmetric with respect to the horizontal? The previously observed mechanism is *a priori* no longer possible and the question arises as to whether a mean flow can still occur. To answer this

https://doi.org/10.1017/jfm.2025.10930 Published online by Cambridge University Press

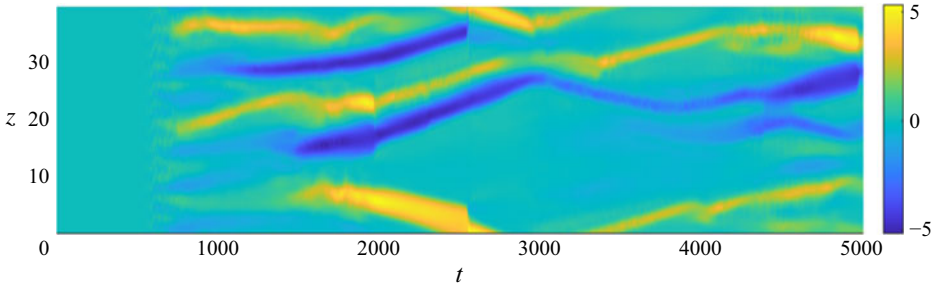


Figure 21. Same as figure 4, but with the forcing (7.1).

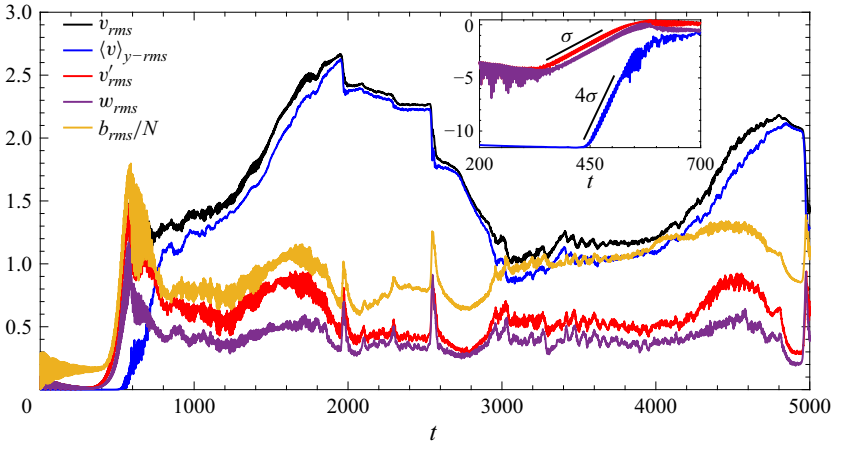


Figure 22. Same as figure 5, but with the forcing (7.1).

question, we have truncated the forcing to

$$q(y, z) = -\frac{q_0}{2}\cos(k_{yf}y + k_{zf}z), \tag{7.1}$$

so that the forced wavevectors are now only $\pm\boldsymbol{k}_{f+}$.

Figure 21 shows a space–time diagram of a simulation with such forcing for the same parameters as the simulation described in § 3: $F_h = 0.4$, $Re = 8840$ and $k_{yf} = k_{zf} = 4k_0$. We can see that layers do arise around the same time as before, but their dynamics is more erratic and their distribution on the vertical is less uniform than in figure 4. Furthermore, they wander along the vertical and can disappear more abruptly.

As seen in figure 22, the r.m.s. of the horizontal mean flow $\langle v\rangle_y$ is again largely dominant relative to the r.m.s. of the fluctuations v'. However, it exhibits larger fluctuations than in figure 5. We can also remark that the average levels of the r.m.s. of v' and w are approximately half those in figure 5. Interestingly, the inset in figure 22 shows that $\langle v\rangle_{y-rms}$ grows initially exponentially with a growth rate that is four times that of v'_{rms}, instead of two times in figure 5.

To understand these results, figure 23 shows the amplitudes of the Fourier modes of v at $t = 550$. We can see that only the discrete wavenumbers aligned along oblique lines $k_z/k_0 = 12n - 2k_y/k_0$, where n is an integer, are non-zero at that time. The first line (i.e. $n = 1$) corresponds to wavevectors $\boldsymbol{k} = \boldsymbol{k}_{f+} + p\boldsymbol{k}_{2+}$, where p is an integer, generated by $p - 1$ quadratic interactions of $\boldsymbol{k}_{2+} = (-k_0, 2k_0)$ with itself and one interaction with

https://doi.org/10.1017/jfm.2025.10930 Published online by Cambridge University Press

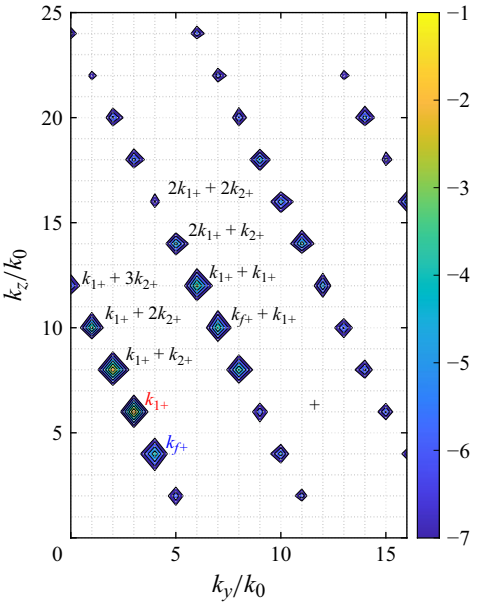


Figure 23. Amplitudes of the Fourier modes $\hat{v}$ of the horizontal velocity with the forcing (7.1) at $t = 550$ for $F_h = 0.4$, $Re = 8840$ and $k_{yf} = k_{zf} = 4k_0$. The colour scale is given in natural logarithm. The wavevectors labelled $\boldsymbol{k}_{1+}$, $\boldsymbol{k}_{f+}$ are the resonant wavevectors. They drive the other wavevectors that are all non-resonant. The evolutions of the labelled wavevectors are displayed in figure 24.

the forced wavevector $\boldsymbol{k}_{f+} = (4k_0, 4k_0)$. Hence, the first interaction $p = 1$ leads to the resonant wavevector $\boldsymbol{k}_{1+} = (3k_0, 6k_0)$, whereas subsequent non-resonant interactions, $p = 2, 3, 4, \ldots$, force non-resonant wavevectors with a decreasing horizontal wavenumber: $(2k_0, 8k_0)$, $(k_0, 10k_0)$, $(0, 12k_0)$ and so on.

As seen in figure 24(a), the growth rate of these successive forced modes is $p\sigma$, where σ is the growth rate of the resonant modes. Hence, four successive nonlinear interactions can generate a non-resonant mode with a zero horizontal wavenumber that grows at a rate 4σ. This explains why $\langle v \rangle_{y-rms}$ in figure 22 grows exponentially with a growth rate four times that of v'_{rms}. Similarly, the modes along the next oblique lines ($n > 1$) can be produced from those of the first line by additional $n - 1$ nonlinear interactions with $\boldsymbol{k}_{1+}$: $\boldsymbol{k} = \boldsymbol{k}_{f+} + p\boldsymbol{k}_{2+} + (n-1)\boldsymbol{k}_{1+}$. A given line n will then produce the shear mode $(0, 12nk_0)$. Figure 24(b) shows that all the other shear modes, i.e. those different from $(0, 12nk_0)$, grow only later and at a different growth rate, probably as a consequence of a secondary triadic instability of the modes produced by the primary instability.

By writing the shear mode $\boldsymbol{k}_v = (0, 12k_0)$ as $\boldsymbol{k}_v = \boldsymbol{k}_{1+} + 3\boldsymbol{k}_{2+}$, the resonance condition (5.5) can be rewritten in terms of a sextet resonance:

$$\boldsymbol{k}_v = \boldsymbol{k}_{f+} + \boldsymbol{k}_{2+} + \boldsymbol{k}_{2+} + \boldsymbol{k}_{2+} + \boldsymbol{k}_{2+}, \tag{7.2a}$$

$$\omega_v = \omega_{f+} + \omega_{2+} \pm \omega_{2+} \pm \omega_{2+} \pm \omega_{2+}, \tag{7.2b}$$

where $\omega_v = 0$ and the sign of the frequencies $\pm\omega_{2+}$ in (7.2b) can be chosen so that the temporal resonance condition is satisfied.

In summary, shear modes are generated by quadratic interactions between enslaved non-resonant modes (Newell, Passot & Lega 1993; Manneville 2014) as before even if the precise mechanism is different from that described in the previous sections. For arbitrary forcing wavenumber (k_{yf}, k_{zf}) and a pair of resonant wavevectors $\boldsymbol{k}_1 = (n_1, m_1)k_0$, $\boldsymbol{k}_2 = (n_2, m_2)k_0$, this mechanism should generate a shear mode after $p = -n_2/M$ interactions

https://doi.org/10.1017/jfm.2025.10930 Published online by Cambridge University Press

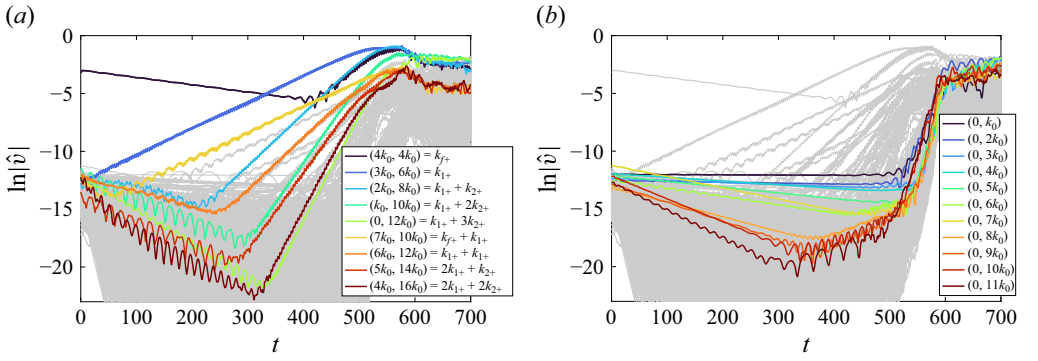


Figure 24. Evolution of the amplitudes of the modes (grey lines) in the wavenumber ranges [0,24k_0]x[0,24k_0] for $F_h = 0.4$, $Re = 8840$ and $k_{yf} = k_{zf} = 4k_0$ with the forcing (7.1). In panel (a), the modes labelled in figure 23 are plotted in colour. In panel (b), all the shear modes $(0, k_z)$ with $0 < k_z \leqslant 11k_0$ are highlighted in colour. The y-axis corresponds to natural logarithm. A moving average over a time interval $\Delta t = 5$ has been applied to filter rapid oscillations.

of the wavevector $\boldsymbol{k}_1$ and $q = n_1/M$ interactions of the wavevector $\boldsymbol{k}_2$, where M is the greatest common divisor of (n_1, n_2), since

$$pk_{1y} + qk_{2y} = 0. \tag{7.3}$$

Then, the shear mode $(0,\ pk_{1z} + qk_{2z})$ will grow at rate $(p + q)\sigma$. An additional condition to have a steady and large forced response is that $(p + q)$ should be even. This ensures that the forcing of shear modes can contain one contribution with zero frequency, i.e. corresponding to their natural frequency.

Finally, it is worth pointing out that even if the shear modes can grow twice as fast by the sextet mechanism compared with the quartet mechanism, the former mechanism was not visible in the simulations with two pairs of forced wavevectors $(\pm\boldsymbol{k}_{f+}, \pm\boldsymbol{k}_{f-})$. Comparing figures 24($a$) and 13($c$), we can see that the initial amplitude of the common shear mode $(0, 12k_0)$, which is amplified by the two mechanisms, is much smaller when the forcing consists of a single pair of forced wavevectors, $\exp(-22) \approx 3.10^{-10}$, than with two pairs, $\exp(-17) \approx 4.10^{-8}$, when it starts to grow exponentially. The exponential growth begins also later in the first case: $t_i \simeq 300$ (figure 24a) than in the second case: $t_i \simeq 200$ (figure 13c). Hence, in figure 13(c), the potential growth at rate 4σ is masked by the growth at rate 2σ since the latter begins before and from a larger amplitude.

8. Conclusion

We have performed direct numerical simulations of the dynamics of a two-dimensional strongly stratified flow in a square periodic domain forced in the momentum equation by a steady mode with vorticity of the form $\sin(k_{yf}y)\sin(k_{zf}z)$. Various values of the forcing wavenumbers have been investigated in the ranges $2k_0 \leqslant k_{yf} \leqslant 5k_0$, $2k_0 \leqslant k_{zf} \leqslant 5k_0$, but we have first investigated in detail the values $k_{yf} = k_{zf} = 4k_0$. For this case, starting from small random noise velocity perturbations, the flow evolves spontaneously towards turbulence and exhibits a horizontal mean flow varying along the vertical. The initial growth of the horizontal mean flow is exponential with a growth rate twice that of the velocity fluctuations. Initially, the horizontal layers are rather regularly distributed with a thickness corresponding typically to half a wavelength of the forcing. However, later on, their size tends to increase and their distribution becomes irregular. Such evolution has been found to occur for a wide range of the forcing intensity and for different values

https://doi.org/10.1017/jfm.2025.10930 Published online by Cambridge University Press

of the buoyancy frequency and viscosity. The root mean squares of the horizontal mean flow and of the velocity fluctuations non-dimensionalised by Nl_0 depend mostly on the Froude number F_h and not on the Reynolds number Re. The flows have similar kinetic and potential energy spectra as two-dimensional strongly stratified turbulence generated by random stochastic forcing (Smith 2001; Kumar *et al.* 2017; Fitzgerald & Farrell 2018*a*; Linares 2020).

Thanks to the use of a deterministic forcing, we have been able to provide clear evidence for the mechanisms leading to the emergence of layers and the transition to turbulence. The detailed analysis of the evolutions of the different Fourier modes of the horizontal velocity shows that a triadic instability involving the forced wavevectors $(\pm k_{yf}, \pm k_{zf})$ first occurs. It is slightly different from the classical triadic instability of weak internal waves because the forced mode is not oscillating at its natural frequency but is steady. As is well known, a mean flow cannot be generated directly by such triadic instability. However, the growth of the resonant internal waves is accompanied by the amplification of six non-resonant enslaved modes at the same growth rate for each triad. Then, the quadratic interactions between the latter modes from two different triads involving forced wavevectors that are symmetric with respect to the horizontal can generate a mean horizontal flow varying along the vertical. Accordingly, these shear modes grow exponentially at a rate twice those of the primary resonant internal waves as observed in the numerical simulations. Such a mechanism is equivalent to the resonant quartet mechanism proposed by Newell (1969) and Smith & Waleffe (1999) for inertial waves in rotating turbulence and Rossby waves in β-plane turbulence. However, resonant quartets were only suspected to be one possible mechanism among others, such as near-resonances, to explain the emergence of a mean flow. Here, the use of deterministic forcing has allowed us to provide clear evidence for its role. It should be also noted that resonant quartets differ significantly from the quartetic instability evidenced by Brunet *et al.* (2020) in experiments on wave-driven rotating turbulence. The latter instability is a secondary instability of the triadic instability when some wavevectors parallel to the primary resonant wavevectors and to the forced wavevectors have a sufficient amplitude. They can emerge in these experiments because it is the frequency of the forcing that is imposed, i.e. the direction of the forced wavevector is fixed, but not its norm. In contrast, resonant quartets are not a secondary instability of the triadic instabilities, but are a nonlinear mechanism associated with the triadic instabilities leading to the growth of enslaved non-resonant modes. We expect that the same phenomenon could occur if an internal wave were forced instead of a steady mode.

The same scenario has been observed for most other values of the forcing wavenumbers (k_{yf}, k_{zf}). However, there exist values for which no triadic instability occurs. Accordingly, the flow then simply evolves towards the forced solution (2.4). One case has been also observed where two distinct pairs of internal waves are unstable with close growth rates. In addition to the previous mechanism, some shear modes can then be generated via the mutual interactions between resonant and non-resonant modes of the two triads. Paradoxically, the mean flow has been observed to be weaker than the fluctuations in the statistically steady regime for this case.

In a second step, we have restricted the forcing to only the form $\cos(k_{yf}y + k_{zf}z)$ such that there are no forced wavevectors that are symmetric with respect to the horizontal. In this case, the previous mechanism is no longer possible. However, the numerical simulations for $k_{yf} = k_{zf} = 4k_0$ still exhibit the emergence of a mean flow, but growing exponentially at a growth rate four times that of the resonant internal waves. The analysis of the evolutions of the different Fourier modes show that four successive quadratic interactions between non-resonant and resonant modes lead to the generation of a mean

https://doi.org/10.1017/jfm.2025.10930 Published online by Cambridge University Press

flow at a growth rate four times the growth rate of the primary triadic instability. This can be interpreted in terms of a sextet resonance. Thus, resonant quartet is only a special case of a more general mechanism by which shear modes are generated via forced non-resonant modes.

For arbitrary values of (k_{yf}, k_{zf}), a similar scenario should always be possible provided that a triadic instability occurs. However, the number n of successive quadratic interactions needed for the generation of shear modes will depend on each case. Accordingly, the growth rate of the shear modes will be $n\sigma$, where σ is the growth rate of the primary triadic instability.

Therefore, for the two types of forcing studied herein, shear modes, i.e. VSHF, are spontaneously generated by the interactions between non-resonant modes driven by triadic instabilities. Such uprising of enslaved modes is able to efficiently channel energy from the resonant modes towards the mean flow. As pointed out by Remmel *et al.* (2014), this mechanism is absent in weak turbulence theories since only resonant interactions are considered. Nevertheless, the link between the present simulations with a steady monochromatic forcing and those using random forcing remains to be made, as shear modes do not appear to grow exponentially in the latter simulations. This could be due to the fact that all wavevector directions in a given wavenumber band are forced randomly, so that a given wavevector is only forced intermittently. However, further investigations would be needed to prove this.

Furthermore, the interactions between non-resonant modes explain the initial emergence of shear modes, but other mechanisms may be responsible for their maintenance and subsequent evolution such as the statistical instability of homogeneous stratified turbulence (Fitzgerald & Farrell 2018*a*, 2018*b*). Hence, we believe that these different mechanisms are complementary.

In the future, it would be interesting to study along the same lines three-dimensional stratified turbulence and different types of turbulence such as two-dimensional β-plane turbulence or rotating turbulence. Three-dimensional stratified turbulence is expected to be more complicated than the present configuration since shear modes are not constrained to a single horizontal direction and there exist potential vorticity modes.

Acknowledgements. We thank M. Le Bars, B. Favier and B. Gallet for insightful discussions, V. Toai for technical assistance and the anonymous referees for their comments that have improved the manuscript.

Funding. A part of this work was performed using HPC resources from GENCI-IDRIS (Grant 2022-AD012A07419R1).

Declaration of interests. The authors report no conflict of interest.

Appendix. Stability analysis

To study the stability of the base solution (2.4), it is first convenient to non-dimensionalize (2.1) by taking $1/N$ and l_0 as time and length units. Accordingly, the streamfunction and buoyancy are non-dimensionalized by Nl_0^2 and $N^2 l_0$, respectively. Then, (2.1) can be rewritten in the form

$$\frac{\partial \tilde{\Delta}\tilde{\psi}}{\partial \tilde{t}} + J(\tilde{\psi}, \tilde{\Delta}\tilde{\psi}) = \frac{\partial \tilde{b}}{\partial \tilde{y}} + \frac{F_h}{Re}\tilde{\Delta}^2\tilde{\psi} + \frac{q}{N^2}, \tag{A1a}$$

$$\frac{\partial \tilde{b}}{\partial \tilde{t}} + J(\tilde{\psi}, \tilde{b}) = -\frac{\partial \tilde{\psi}}{\partial \tilde{y}} + \frac{F_h}{ReSc}\tilde{\Delta}\tilde{b}, \tag{A1b}$$

where $J(.,.) = \partial./\partial\tilde{y}\partial./\partial\tilde{z} - \partial./\partial\tilde{z}\partial./\partial\tilde{y}$ is the Jacobian and tilded quantities are non-dimensional.

https://doi.org/10.1017/jfm.2025.10930 Published online by Cambridge University Press

Then, the base solution (2.4), taken at leading order in q_0 for $t \to \infty$ and non-dimensionalised as done previously, can be decomposed as the sum of four modes:

$$\begin{pmatrix} \tilde{\psi} \\ \tilde{b} \end{pmatrix} = \begin{pmatrix} \tilde{\psi}_+ \\ \tilde{b}_+ \end{pmatrix} e^{(\mathrm{i}\tilde{k}_{yf}\tilde{y}+\mathrm{i}\tilde{k}_{zf}\tilde{z})} + c.c. + \begin{pmatrix} \tilde{\psi}_- \\ \tilde{b}_- \end{pmatrix} e^{(\mathrm{i}\tilde{k}_{yf}\tilde{y}-\mathrm{i}\tilde{k}_{zf}\tilde{z})} + \mathrm{c.c.}, \tag{A2}$$

where $\tilde{\psi}_+ = -\tilde{\psi}_- = -q_0\gamma/(4Nl_0^2)$, $\tilde{b}_+ = -\tilde{b}_- = -\mathrm{i}q_0\beta/(4N^2 l_0)$. This shows that the non-dimensional base buoyancy and streamfunction scale as $\tilde{b}_s = O(F_h^2)$ and $\tilde{\psi}_s = O(F_h^3/Re)$ with $s = \{+, -\}$. By assuming the distinguished scaling $Re = \widetilde{Re}/F_h$, we can write $\tilde{b}_s = F_h^2 B_s$ and $\tilde{\psi}_s = F_h^4 \Psi_s$, where capital quantities are assumed to be of order unity. The total perturbations are scaled similarly: $\tilde{b} = F_h^2 B$ and $\tilde{\psi} = F_h^4 \Psi$.

Therefore, the stability problem can be solved asymptotically with F_h^2 as a small parameter following weakly interacting wave theories (LeBlond & Mysak 1981; Bouruet-Aubertot et al. 1995; Staquet & Sommeria 2002; Dauxois *et al.* 2018). The time and the infinitesimal perturbations are expanded with the Froude number as follows: $\partial/\partial\tilde{t} = \partial/\partial t_0 + F_h^2\partial/\partial t_1 + \ldots$ and

$$\begin{pmatrix} \psi' \\ b' \end{pmatrix} = \begin{pmatrix} \psi'_0 \\ b'_0 \end{pmatrix} + F_h^2 \begin{pmatrix} \psi'_1 \\ b'_1 \end{pmatrix} + \ldots. \tag{A3}$$

Introducing the infinitesimal perturbations (A3) into (A1) leads at leading order to

$$\frac{\partial \tilde{\Delta}\psi'_0}{\partial t_0} = \frac{\partial b'_0}{\partial \tilde{y}}, \tag{A4a}$$

$$\frac{\partial b'_0}{\partial t_0} = -\frac{\partial \psi'_0}{\partial \tilde{y}}. \tag{A4b}$$

The solution is taken in the form

$$\begin{pmatrix} \psi'_0 \\ b'_0 \end{pmatrix} = \begin{pmatrix} \psi'_{01}(t_1) \\ b'_{01}(t_1) \end{pmatrix} e^{(\mathrm{i}\tilde{k}_{y1}\tilde{y}+\mathrm{i}\tilde{k}_{z1}\tilde{z}-\mathrm{i}\tilde{\omega}_1 t_0)} + \begin{pmatrix} \psi'_{02}(t_1) \\ b'_{02}(t_1) \end{pmatrix} e^{(\mathrm{i}\tilde{k}_{y2}\tilde{y}+\mathrm{i}\tilde{k}_{z2}\tilde{z}-\mathrm{i}\tilde{\omega}_2 t_0)}, \tag{A5}$$

where $\tilde{\omega}_1$ and $\tilde{\omega}_2$ satisfy the dispersion relation (5.6) in non-dimensional form.

At order F_h^2, we get

$$\frac{\partial \tilde{\Delta}\psi'_1}{\partial t_0} - \frac{\partial b'_1}{\partial \tilde{y}} = -\frac{\partial \tilde{\Delta}\psi'_0}{\partial t_1} + \frac{1}{\tilde{Re}}\tilde{\Delta}^2\psi'_0, \tag{A6a}$$

$$\frac{\partial b'_1}{\partial t_0} + \frac{\partial \psi'_1}{\partial \tilde{y}} = -\frac{\partial b'_0}{\partial t_1} - J(\psi'_0, B) + \frac{1}{\tilde{Re}S_c}\tilde{\Delta}b'_0. \tag{A6b}$$

If the resonance conditions (5.5) are satisfied for the Fourier components associated with B_+, the compatibility conditions to be able to solve these equations are

$$\frac{\partial \psi'_{01}}{\partial t_1} = -\frac{1}{2\tilde{Re}}\tilde{k}_1^2\left(1+\frac{1}{S_c}\right)\psi'_{01} - \frac{\tilde{\omega}_1\tilde{\alpha}}{2\tilde{k}_{y1}}\psi'_{02}B_+ e^{2\mathrm{i}\delta_\omega t_1}, \tag{A7}$$

$$\frac{\partial \psi'_{02}}{\partial t_1} = -\frac{1}{2\tilde{Re}}\tilde{k}_2^2\left(1+\frac{1}{S_c}\right)\psi'_{02} + \frac{\tilde{\omega}_2\tilde{\alpha}}{2\tilde{k}_{y2}}\psi'_{01}B_+^* e^{-2\mathrm{i}\delta_\omega t_1}, \tag{A8}$$

where $\tilde{k}_j = \|\tilde{\boldsymbol{k}}_j\|$ and $\tilde{\alpha} \equiv \tilde{k}_{yf}\tilde{k}_{z1} - \tilde{k}_{zf}\tilde{k}_{y1} = \tilde{k}_{yf}\tilde{k}_{z2} - \tilde{k}_{zf}\tilde{k}_{y2}$ because of (5.5*a*). In (A7)–(A8), it has been assumed that the resonance condition (5.5*b*) could be not satisfied exactly by introducing the detuning parameter $\tilde{\delta}_\omega = (\tilde{\omega}_1 - \tilde{\omega}_2)/2$. By assuming that this parameter

https://doi.org/10.1017/jfm.2025.10930 Published online by Cambridge University Press

is small such that $\tilde{\delta}_\omega = \delta_\omega F_h^2$ with $\delta_\omega = O(1)$, we have rewritten the phase shift in terms of the slow time t_1: $\tilde{\delta}_\omega t_0 = \delta_\omega t_1$.

By writing $\psi'_{01} = \psi_{01}\exp(\tilde{\sigma}t_1 + \mathrm{i}\delta_\omega t_1)$ and $\psi'_{02} = \psi_{02}\exp(\tilde{\sigma}t_1 - \mathrm{i}\delta_\omega t_1)$, and by rescaling the growth rate $\sigma = NF_h^2\tilde{\sigma}$ and all the other variables, we obtain in dimensional form, i.e. in terms of untilded quantities,

$$\sigma = -\frac{\nu}{4}\left(1+\frac{1}{S_c}\right)\left(k_1^2+k_2^2\right) \pm \frac{1}{4}\sqrt{\left(\nu\left(1+\frac{1}{S_c}\right)\left(k_1^2-k_2^2\right)+2\mathrm{i}(\omega_1-\omega_2)\right)^2 - \frac{4\alpha^2|b_+|^2\omega_1\omega_2}{N^4 k_{y1}k_{y2}}}. \tag{A9}$$

The destabilisation being due to the last term of (A9), we see that a necessary condition for instability when the resonance is exact, $\omega_1 = \omega_2$, is that k_{y1} and k_{y2} be of opposite sign so that this term is positive.

The same expression is obtained when considering (b_-, ψ_-) except the changes $k_{zf} \to -k_{zf}$ and $b_+ \to b_-$.

References

Augier, P., Billant, P. & Chomaz, J.-M. 2015 Stratified turbulence forced with columnar dipoles: numerical study. *J. Fluid Mech.* **769**, 403–443.

Benielli, D. & Sommeria, J. 1998 Excitation and breaking of internal gravity waves by parametric instability. *J. Fluid Mech.* **374**, 117–144.

Bouruet-Aubertot, P., Sommeria, J. & Staquet, C. 1995 Breaking of standing internal gravity waves through two-dimensional instabilities. *J. Fluid Mech.* **285**, 265–301.

Bouruet-Aubertot, P., Sommeria, J. & Staquet, C. 1996 Stratified turbulence produced by internal wave breaking: two-dimensional numerical experiments. *Dyn. Atmos. Oceans* **23** (1-4), 357–369.

Brethouwer, G., Billant, P., Lindborg, E. & Chomaz, J.-M. 2007 Scaling analysis and simulation of strongly stratified turbulent flows. *J. Fluid Mech.* **585**, 343–368.

Brunet, M., Gallet, B. & Cortet, P.-P. 2020 Shortcut to geostrophy in wave-driven rotating turbulence: the quartetic instability. *Phys. Rev. Lett.* **124** (12), 124501.

de Bruyn Kops, S.M. & Riley, J.J. 1998 Direct numerical simulation of laboratory experiments in isotropic turbulence. *Phys. Fluids* **10** (9), 2125–2127.

Caulfield, C.P. 2021 Layering, instabilities, and mixing in turbulent stratified flows. *Annu. Rev. Fluid Mech.* **53**, 113–145.

Dauxois, T., Joubaud, S., Odier, P. & Venaille, A. 2018 Instabilities of internal gravity wave beams. *Annu. Rev. Fluid Mech.* **50**, 131–156.

Deloncle, A. 2007 Three dimensional instabilities in stratified fluids. PhD thesis, Ecole Polytechnique.

Deloncle, A., Billant, P. & Chomaz, J.-M. 2008 Nonlinear evolution of the zigzag instability in stratified fluids: a shortcut on the route to dissipation. *J. Fluid Mech.* **599**, 229–239.

Farrell, B.F. & Ioannou, P.J. 2019 Statistical state dynamics: a new perspective on turbulence in shear flow. In *Zonal Jets Phenomenology, Genesis, and Physics*.(ed. B. Galpirin and P. L. Read), pp. 380–400. Cambridge University Press.

Fitzgerald, J.G. & Farrell, B.F. 2018*a* Statistical state dynamics of vertically sheared horizontal flows in two-dimensional stratified turbulence. *J. Fluid Mech.* **854**, 544–590.

Fitzgerald, J.G. & Farrell, B.F. 2018*b* Vertically sheared horizontal flow-forming instability in stratified turbulence: analytical linear stability analysis of statistical state dynamics equilibria. *J. Atmos. Sci.* **75** (12), 4201–4227.

Galmiche, M., Thual, O. & Bonneton, P. 2000 Wave/wave interaction producing horizontal mean flows in stably stratified fluids. *Dyn. Atmos. Oceans* **31** (1–4), 193–207.

Galperin, B. & Read, P.L. 2019 *Zonal Jets: Phenomenology, Genesis, and Physics*. Cambridge University Press.

Herbert, C., Marino, R., Rosenberg, D. & Pouquet, A. 2016 Waves and vortices in the inverse cascade regime of stratified turbulence with or without rotation. *J. Fluid Mech.* **806**, 165–204.

Herring, J.R. & Métais, O. 1989 Numerical experiments in forced stably stratified turbulence. *J. Fluid Mech.* **202**, 97–115.

https://doi.org/10.1017/jfm.2025.10930 Published online by Cambridge University Press

KOUDELLA, C.R. & STAQUET, C. 2006 Instability mechanisms of a two-dimensional progressive internal gravity wave. *J. Fluid Mech.* **548**, 165–196.
KUMAR, A., VERMA, K.M. & SUKHATME, J. 2017 Phenomenology of two-dimensional stably stratified turbulence under large-scale forcing. *J. Turbul.* **18** (3), 219–239.
LAVAL, J.-P., MCWILLIAMS, J.C. & DUBRULLE, B. 2003 Forced stratified turbulence: successive transitions with Reynolds number. *Phys. Rev. E* **68** (3), 036308.
LE REUN, T., GALLET, B., FAVIER, B. & LE BARS, M. 2020 Near-resonant instability of geostrophic modes: beyond Greenspan's theorem. *J. Fluid Mech.* **900**, R2.
LEBLOND, P.H. & MYSAK, L.A. 1981 *Waves in the Ocean*. Elsevier.
LELONG, M.-P. & RILEY, J.J. 1991 Internal wave – vortical mode interactions in strongly stratified flows. *J. Fluid Mech.* **232**, 1–19.
LEMASQUERIER, D., FAVIER, B. & LE BARS, M. 2021 Zonal jets at the laboratory scale: hysteresis and Rossby waves resonance. *J. Fluid Mech.* **910**, A18.
LINARES, M.C. 2020 Numerical study of 2d stratified turbulence forced by internal gravity waves. PhD thesis, Université Grenoble Alpes.
LINDBORG, E. 2006 The energy cascade in a strongly stratified fluid. *J. Fluid Mech.* **550**, 207–242.
MAFFIOLI, A. 2019 Asymmetry of vertical buoyancy gradient in stratified turbulence. *J. Fluid Mech.* **870**, 266–289.
MAFFIOLI, A., BRETHOUWER, G. & LINDBORG, E. 2016 Mixing efficiency in stratified turbulence. *J. Fluid Mech.* **794**, R3.
MANNEVILLE, P. 2014 *Dissipative Structures and Weak Turbulence*. Academic Press.
MCEWAN, A.D. 1971 Degeneration of resonantly-excited standing internal gravity waves. *J. Fluid Mech.* **50** (3), 431–448.
MCEWAN, A.D., MANDER, D.W. & SMITH, R.K. 1972 Forced resonant second-order interaction between damped internal waves. *J. Fluid Mech.* **55** (4), 589–608.
NEWELL, A.C. 1969 Rossby wave packet interactions. *J. Fluid Mech.* **35** (2), 255–271.
NEWELL, A.C., PASSOT, T. & LEGA, J. 1993 Order parameter equations for patterns. *Annu. Rev. Fluid Mech.* **25**, 399–453.
PHILLIPS, O.M. 1968 The interaction trapping of internal gravity waves. *J. Fluid Mech.* **34** (2), 407–416.
PHILLIPS, O.M. 1972 Turbulence in a strongly stratified fluid – is it unstable? *Deep Sea Res.* **19** (1), 79–81.
PLUMB, R.A. & MCEWAN, A.D. 1978 The instability of a forced standing wave in a viscous stratified fluid: a laboratory analogue of the quasi-biennial oscillation. *J. Atmos. Sci.* **35** (10), 1827–1839.
POSMENTIER, E.S. 1977 The generation of salinity finestructure by vertical diffusion. *J. Phys. Oceanogr.* **7** (2), 298–300.
REMMEL, M., SUKHATME, J. & SMITH, L.M. 2014 Nonlinear gravity-wave interactions in stratified turbulence. *Theor. Comput. Fluid Dyn.* **28**, 131–145.
RHINES, P.B. 1975 Waves and turbulence on a beta-plane. *J. Fluid Mech.* **69** (3), 417–443.
RILEY, J.J. & LELONG, M.-P. 2000 Fluid motions in the presence of strong stable stratification. *Annu. Rev. Fluid Mech.* **32** (1), 613–657.
SEMIN, B., FACCHINI, G., PÉTRÉLIS, F. & FAUVE, S. 2016 Generation of a mean flow by an internal wave. *Phys. Fluids* **28** (9), 096601.
SEMIN, B., GARROUM, N., PÉTRÉLIS, F. & FAUVE, S. 2018 Nonlinear saturation of the large scale flow in a laboratory model of the quasibiennial oscillation. *Phys. Rev. Lett.* **121** (13), 134502.
SMITH, L.M. 2001 Numerical study of two-dimensional stratified turbulence. *Contemp. Math.* **283**, 91–106.
SMITH, L.M. & WALEFFE, F. 1999 Transfer of energy to two-dimensional large scales in forced, rotating three-dimensional turbulence. *Phys. Fluids* **11** (6), 1608–1622.
SMITH, L.M. & WALEFFE, F. 2002 Generation of slow large scales in forced rotating stratified turbulence. *J. Fluid Mech.* **451**, 145–168.
SRINIVASAN, K. & YOUNG, W.R. 2012 Zonostrophic instability. *J. Atmos. Sci.* **69** (5), 1633–1656.
STAQUET, C. & SOMMERIA, J. 2002 Internal gravity waves: from instabilities to turbulence. *Annu. Rev. Fluid Mech.* **34** (1), 559–593.
SUTHERLAND, B.R. 2010 *Internal Gravity Waves*. Cambridge University Press.
THORPE, S.A. 1968 On standing internal gravity waves of finite amplitude. *J. Fluid Mech.* **32** (3), 489–528.
WAITE, M.L. & BARTELLO, P. 2004 Stratified turbulence dominated by vortical motion. *J. Fluid Mech.* **517**, 281–308.
WEDI, N.P. & SMOLARKIEWICZ, P.K. 2006 Direct numerical simulation of the Plumb–McEwan laboratory analog of the QBO. *J. Atmos. Sci.* **63** (12), 3226–3252.

https://doi.org/10.1017/jfm.2025.10930 Published online by Cambridge University Press